



An Active–Passive Microwave Land Surface Database From GPM

S. Joseph Munchak, Sarah Ringerud, Ludovic Brucker, Yalei You, Iris de
Gelís, Catherine Prigent

► To cite this version:

S. Joseph Munchak, Sarah Ringerud, Ludovic Brucker, Yalei You, Iris de Gelís, et al.. An Active–Passive Microwave Land Surface Database From GPM. *IEEE Transactions on Geoscience and Remote Sensing*, 2020, 58 (9), pp.6224-6242. 10.1109/TGRS.2020.2975477 . hal-03045732

HAL Id: hal-03045732

<https://hal.sorbonne-universite.fr/hal-03045732v1>

Submitted on 1 Mar 2023

HAL is a multi-disciplinary open access archive for the deposit and dissemination of scientific research documents, whether they are published or not. The documents may come from teaching and research institutions in France or abroad, or from public or private research centers.

L'archive ouverte pluridisciplinaire **HAL**, est destinée au dépôt et à la diffusion de documents scientifiques de niveau recherche, publiés ou non, émanant des établissements d'enseignement et de recherche français ou étrangers, des laboratoires publics ou privés.

An Active-Passive Microwave Land Surface Database from GPM

S. Joseph Munchak, Sarah Ringerud, Ludovic Brucker, Yalei You, Iris de Gelis, Catherine Prigent

Abstract—A microwave emissivity retrieval is applied to five years of Global Precipitation Measurement (GPM) Microwave Imager (GMI) observations over land and sea ice. The emissivities are co-located with GPMs Dual-frequency Precipitation Radar (DPR) surface backscatter measurements in clear-sky conditions. The emissivity-backscatter database is used to characterize surfaces within the GPM orbit for precipitation retrieval algorithms and other applications.

The full 10-166 GHz emissivity vector is retrieved using optimal estimation. Since GMI includes water vapor sounding channels, retrieval of the atmospheric and surface state are performed simultaneously. Using the MERRA2 reanalysis as the a priori atmospheric state and with proper characterization of its error, we are able to effectively screen for cloud- and precipitation-affected emissivities. Comparisons with co-located CloudSat data show that this GMI-based screen is able to detect precipitation that DPR alone does not; however, about 10% of precipitation occurrence from CloudSat is still undetected by GMI.

The unsupervised Kohonen classification technique was then applied to multi-year monthly 0.25° gridded mean retrieved emissivities and backscatter distinctly for snow-free, snow-covered, and sea ice surfaces in order to classify surfaces based on both active and passive microwave characteristics. The classes correspond to vegetation coverage and type, inundation zones, soil composition, and terrain roughness. Snow and sea ice surfaces show clear seasonal cycles representing the increase in snow and ice spatial extent and reduction in the spring. Applications toward GPM precipitation retrieval algorithms and sensitivity to accumulated rain and snowfall are also explored.

I. INTRODUCTION

S.J.Munchak is with the Mesoscale Atmospheric Processes Laboratory, NASA Goddard Space Flight Center, 8800 Greenbelt Road, Greenbelt, MD 20771 e-mail: s.j.munchak@nasa.gov.

Manuscript received 16 August 2019.

THE widespread use of microwave radiometry to retrieve precipitation globally [1]–[3], and assimilation into numerical weather prediction models [4]–[7] including their land surface model components [8]–[11], require the ability to accurately represent the surface emissivity across the microwave spectrum (i.e., 10–180 GHz for precipitation applications). Likewise, accurate representation of both the active and passive surface signal is critical for spaceborne estimates of precipitation [12]–[14] and has become important for retrievals of surface properties, such as vegetation water content [15], soil moisture [16], and inundated area fraction [17].

In order to represent microwave surface characteristics for these wide-ranging applications, fully physical forward models, semi-empirical geophysical model functions, and statistical representations may be employed. Fully physical forward models calculate the emission and backscatter at the surface-atmosphere boundary given the vertical profiles of properties at play (e.g., temperature, dielectric constant, roughness spectrum, and scattering properties from vegetation or snow grains). Examples of such models include the Community Radiative Transfer Model Microwave Emissivity Model (CRTM-MEM [18]), Land Surface Microwave Emission Model (LSMEM [19]), Microwave Emission Model for Layered Snowpacks (MEMLS [20]), Dense Media Radiative Transfer - Multi-Layer (DMRT-ML [21]) and the recent model framework for Snow Microwave Radiative Transfer (SMRT [22]). While these models contribute to our enhanced understanding of the sensitivity of emissivity to physical properties, the extensive input parameter set is generally underdetermined with

respect to observations [23]–[25], and particular models may not be able to represent all surfaces [18]. Semi-empirical approaches, sometimes called geophysical model functions, seek to relate (via regression or other statistical methods) a subset of surface properties (e.g., soil moisture, leaf area index, snow water equivalent) to the emissivity/backscatter spectrum, and can be derived from combinations of observations and physical forward models [26]–[29]. The fully statistical approaches do not seek to represent the surface emissivity or backscatter in terms of physical parameters but instead use observations to quantify the relationships between emissivities at various frequencies and incidence angles as covariance matrices or principal components [30], [31]. An example of such an approach is the Tool to Estimate Land Surface Emissivities at Microwave frequencies (TELSEM; [32]), which uses a clustering approach to identify self-similar surfaces (based on the derived means and covariances) on spatial and temporal (monthly) grids. A similar clustering approach based upon statistics of the surface backscatter cross-section from the TRMM Precipitation Radar (PR) was developed by [33].

The precipitation retrieval algorithms for the Global Precipitation Measurement (GPM) mission [34] include passive microwave algorithms for a diverse collection of microwave sounders and imagers [35], including the GPM Microwave Imager (GMI); radar-only algorithms for GPM's Dual-frequency Precipitation Radar (DPR) at Ku- and Ka-band [36]; and an algorithm for combined DPR and GMI-based retrievals [37]. For these algorithms, the existing methods to estimate surface properties meet some, but not all, algorithm needs [38]. The physical and semi-empirical approaches require detailed land surface data that is not reliably available on the global scale, and some fully-physical models impose significant computational burden for use in routine retrievals with large satellite datasets. The TELSEM classes are used to stratify databases for the passive microwave retrievals of precipitation [35], [39], but the actual emissivity atlases and covariances are only used in forward modeling step of the combined algorithm. Because TESLEM

was derived from Special Sensor Microwave/Imager (SSM/I) observations from 19–85 GHz [40], [41], it does not have a basis for the lowest (10.65 GHz) and highest (166–183 GHz) channels on GMI. The DPR and combined algorithms currently use internally-generated atlases of σ_0 over land as a temporal reference [42], but these suffer from poor sampling at any given incidence angle (ranging from 0 to 18° in 0.75° increments), yet fine-resolution grids (ideally, approaching the radar resolution of 5 km) are desirable for this reference method to account for small-scale heterogeneity of the land surface [43].

In order to provide a basis for a statistical joint active-passive surface characterization for the GPM combined precipitation algorithm, as well as to take advantage of the superior resolution, calibration, and frequency range of GMI compared to SSM/I, we have generated a database of co-located retrieved land surface emissivity and measured backscatter cross-section (σ_0) at Ku and Ka bands derived from GPM GMI and DPR observations. While the immediate application of this database is improved precipitation retrievals, it is envisioned that the unique, extensive dataset may motivate further study and evaluation of semi-empirical and fully physical microwave surface models and surface property retrievals. The details of the emissivity retrieval and database construction, including derivation and analysis of the surface-atmosphere state and observation error covariances matrices, which are required for robust estimation of the surface emissivity, are described in section II. An unsupervised classification method is applied in section III. A few examples of applications of this database and classification, including implementation in the GPM precipitation algorithms, are given in section IV. A summary description of the database and classification findings, along with concluding remarks, are given in section V.

II. EMISSIVITY RETRIEVAL

The retrieval of the land surface emissivity from GMI observations is described in this section, beginning with datasets used, retrieval assumptions, and forward model components, fol-

lowed by a description of the process for selecting cloud- and precipitation-free observations. From these retrievals, the active-passive surface emissivity and backscatter database is constructed from GPM swath data to be used for surface classification and other applications.

A. GMI Observations

The observations used to retrieve emissivity are the calibrated, co-registered brightness temperatures from GMI (Level 1C-R). The calibration process is described by [44], who consider the calibration accuracy to be within 0.25 K at all channels. As such, it can be claimed that GMI is the most well-calibrated microwave imager presently making Earth observations and is accordingly used as a reference to intercalibrate other earth-viewing microwave imagers [45].

The feedhorns on GMI are arranged in two rows, at approximately 48.45° off-nadir angle from 10-89 GHz (scan line S1) and 45.28° at 166 and both 183 GHz channels (S2) [46]. As a consequence, the S1 and S2 scan lines trace out arcs of differing radii on the Earth's surface, which intersect at some azimuth angles but can be offset by as much as half of the inter-scan line spacing, which is approximately 13 km from a nominal altitude of 407 km and 32 rpm reflector rotation rate. The resulting 6.5 km offset is larger than the effective field of view (EFOV) at frequencies ≥ 89 GHz (Table I). Therefore, the swath is under-sampled at these frequencies and the S1 and S2 channels do not necessarily sample the same volume. Nevertheless, for emissivity estimation we use the Level 1C-R product which maps the S2 channels to the nearest-neighbor S1 position, allowing co-registered GMI observations to be treated independently, as is the current practice for the GMI rainfall products [35]. This practice effectively assumes that the scene is homogeneous on the scale of the largest footprint (10 GHz). While we could (de)convolve the brightness temperatures so that they are matched on a common footprint before the retrieval, this is only possible at frequencies ≤ 36 GHz [47]. Furthermore, for analysis and classification the emissivities are gridded at 0.25° which is close to the 10 GHz footprint.

B. Retrieval method

The retrieval itself is an implementation of the optimal estimation method [48], which is commonly used for atmospheric sounding either as a pre-processor for data assimilation [6] or a standalone geophysical parameter retrievals [49], [50]. The retrieval is performed by minimizing the cost function

$$\Phi = (\mathbf{Y}_{\text{sim}}(\mathbf{X}) - \mathbf{Y}_{\text{obs}})^T \mathbf{S}_y^{-1} (\mathbf{Y}_{\text{sim}}(\mathbf{X}) - \mathbf{Y}_{\text{obs}}) + (\mathbf{X} - \mathbf{X}_a)^T \mathbf{S}_a^{-1} (\mathbf{X} - \mathbf{X}_a), \quad (1)$$

where \mathbf{Y} is the observation vector, consisting of the co-located GMI brightness temperatures, \mathbf{S}_y is the observation and forward model error covariance matrix, \mathbf{X} is the retrieval geophysical parameter vector, which is constrained by its prior \mathbf{X}_a and its error covariance matrix \mathbf{S}_a . The retrieval outcome depends strongly on the choice of parameters to include in \mathbf{X} and the tightness of the constraints implied by \mathbf{S}_y and \mathbf{S}_a . Since we are interested in surface emissivity estimates under clear-sky conditions, only the parameters that have a significant (relative to channel NEDT) impact on GMI-frequency brightness temperature under these conditions are considered. These parameters include the surface (skin) temperature, atmospheric temperature and water vapor profiles, and the frequency- and polarization-dependent emissivity vector. Surface temperature is of primary importance for retrievals over land covers that have a shallow microwave penetration depth. However, terrestrial snowpacks and some sandy deserts in contrast allow the microwave radiation to penetrate, especially at frequencies ≤ 89 GHz [51]. Therefore, the temperature of the emitting media cannot be independently retrieved from the emissivity vector, and is not the same at all channels due to frequency- and polarization-dependent penetration depths [52]. In the retrieval we fix the surface temperature (T_s) from ancillary data and acknowledge that we are, in essence, retrieving an “effective emissivity” vector (ϵ_{eff}), where the upwelling radiance (R_\uparrow) at the surface at frequency f and polarization p is

$$R_\uparrow(f, p) = T_s \epsilon_{eff}(f, p) + (1 - \epsilon_{eff}(f, p)) R_\downarrow(f, p). \quad (2)$$

TABLE I
SUBSET OF GMI CHANNEL CHARACTERISTICS DESCRIBED BY [46]

Frequency (GHz)	Polarization	EIA (deg)	Beamwidth (deg)	EFOV (km)	NEDT (V) (K)	NEDT (H) K
10.65	V/H	52.8	1.72	20x32	0.77	0.78
18.7	V/H	52.8	0.98	12x18	0.63	0.60
23.8	V	52.8	0.85	10x16	0.51	
36.64	V/H	52.8	0.82	10x15	0.41	0.42
89	V/H	52.8	0.38	6x7	0.32	0.31
166	V/H	49.1	0.38	6x6	0.70	0.65
183±3	V	49.1	0.37	6x5	0.56	
183±7	V	49.1	0.37	6x5	0.47	

Although we know and expect that strong covariances exist between emissivities at the GMI frequencies and polarizations, these are left out of \mathbf{S}_a to avoid over-constraining the result. Indeed, since one of the purposes of developing this database is to discover these covariances (and their covariance with DPR σ_0), the diagonal elements of \mathbf{S}_a representing emissivity are purposely set to the large (unitless) value of 0.25² with zero covariance. The prior values in \mathbf{X}_a are interpolated in angle and frequency from the TELSEM atlas. The emissivity at each GMI frequency and polarization is considered as an independent retrieval parameter, except that the 23.8V emissivity is bounded by the 18.7V and 36.64V estimates (although free to vary within these bounds) and that the emissivity is assumed to not vary between the 166V, 183±7V, and 183±3V. Under most conditions, the high atmospheric opacity at the 183 GHz channels precludes the independent estimation of emissivity for those channels.

The atmospheric temperature and water vapor profiles also have a significant impact on GMI brightness temperatures. Since these profiles are highly variable in space and time, it is beneficial to utilize atmospheric reanalyses that assimilate heterogeneous observing systems with a dynamic model to constrain the atmospheric state. Such analyses provide a more accurate prior constraint on the atmosphere than a static climatology. In this study, we use the NASA Modern-Era Retrospective analysis for Research and Applications, Version

2 (MERRA-2; [53]). The atmospheric temperature and water vapor profile is linearly interpolated in time and space from the 3-hourly, 0.5°x0.625° atmospheric analysis data [54] and the surface (skin) temperature and 2-meter (T_{2m}) are interpolated from the hourly, 0.5°x0.625° surface analysis data [55]. Sensitivity tests showed that the GMI brightness temperatures were not sensitive (at the 0.1 K level) to the atmosphere above 50 hPa, so MERRA-2 profiles were truncated at this level, retaining 27 layers of the original 42. Additionally, the MERRA-2 cloud liquid water path (CLWP), while not used in the retrieval itself, is interpolated to each GMI footprint and used as a input to the screening process, intended to filter out cloud- and precipitation-contaminated retrievals and described later in this section.

As with all reanalyses, MERRA-2 profiles are not without error, particularly with respect to mesoscale features that are smaller than the reanalysis effective resolution [56] or in data-sparse regions¹. These features, which include jet streaks, cyclonic eddies, and convection, can locally alter the atmospheric temperature and water vapor profiles from the larger-scale mean. Thus, we need to derive an accurate characterization of these errors so that \mathbf{S}_a properly constrains the retrieval. To achieve this, approximately 10,000 radiosonde observations, evenly

¹MERRA-2 does not assimilate GMI, so performing GMI-based atmospheric and surface retrievals introduces new information to the knowledge of the state.

sampled throughout the year 2015, were subset from the International Global Radiosonde Archive (IGRA; [57]), Version 2. These were compared to the MERRA-2 data interpolated to the radiosonde location and used to derive the error covariance matrix of MERRA-2 atmospheric temperature (T) and water vapor (expressed in terms of relative humidity – RH) at the 27 MERRA-2 pressure levels ≥ 50 hPa along with T_{2m} . (Figure 1a). It should be noted that, because these radiosonde observations are also input to the MERRA-2 analysis, they do not provide a fully independent assessment of the analysis error. Ideally, non-assimilated observations would be used to derive S_a , but to our knowledge, such a comprehensive yet independent and globally representative dataset does not exist.

The error covariance matrix shown in Figure 1a was then used to derive the empirical orthogonal functions (EOFs) of temperature and relative humidity error, which are shown in Figures 1b-c. These EOFs represent the correlated structure of these errors and are retrieved (along with the effective emissivity vector) in the optimal estimation framework state vector \mathbf{X} . The number of retrieved EOFs was determined by modeling the GMI brightness temperatures (T_b) for each radiosonde profile in the IGRA subset and its corresponding representation as a sum of the MERRA-2 analysis and N_{EOF} error EOFs. Because the variance explained in T-RH space does not necessarily correspond to the variance explained in T_b space, the EOFs were reordered such that the maximum reduction in all-channel T_b root-mean-square error was achieved with each sequential EOF. We also found, through trial and error, that giving RH twice the weight of T (after normalizing by the standard deviation at each level) resulted in a more rapid reduction of the T_b rmse with fewer EOFs than equal T-RH weights, and these weighted EOFs are what is shown in Figure 1b (this result is not altogether surprising, considering that the GMI 183 GHz channels are near a water vapor absorption line). The rmse for each channel is shown as a function of N_{EOF} in Figure 2. The rmse is highest for the high-frequency channels that are more sensitive to the atmospheric state, and decrease with decreasing frequency. We

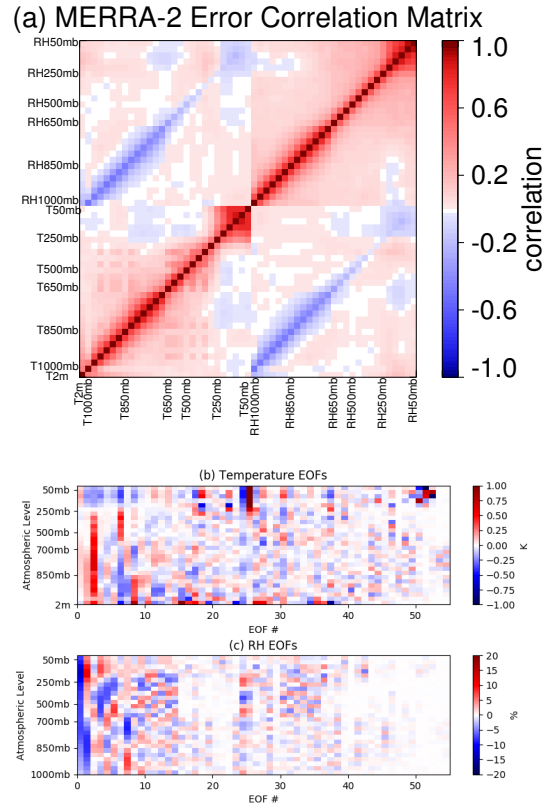


Fig. 1. a) Correlation matrix of MERRA-2 temperature and humidity profile departures from radiosonde observations. b) Temperature and c) relative humidity empirical orthogonal functions derived from the covariance matrix represented in (a).

note an inflection point at $N_{EOF} = 5$ and the error is also less than or comparable to the NEDT at most channels. Thus we choose this value for the retrieval. This process also provides input to the observation + forward model error covariance matrix S_y , which is the residual error covariance from the non-retrieved EOFs plus the channel NEDT (Table I) along the diagonal.

The forward model used to calculate the GMI brightness temperatures accounts for absorption by O_2 , N_2 , and H_2O , but not O_3 (sensitivity tests showed < 0.1 K impact at the most-affected channel, 166 GHz, when integrated over the GMI bandwidth). The extinction coefficients were obtained

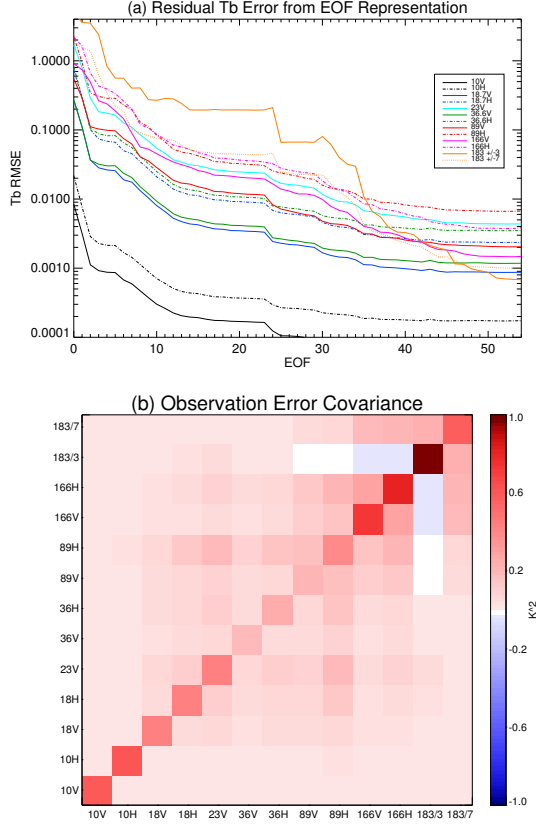


Fig. 2. a) Residual Tb rms error as a function of number of error EOFs used to represent the radiosonde profiles. b) Residual error covariance matrix at $N_{\text{EOF}} = 5$, plus channel NEDT from Table I along the diagonal.

from MonoRTM [58] version 5.3 and integrated over the GMI spectral response function. Surface reflection is assumed to be specular, which should not introduce significant error over snow-free surfaces [59] at the GMI incidence angle [60], [61], although it is important that this assumption be carried forward when using the retrieved emissivities in other applications. The forward model intentionally does not account for scattering by hydrometeors or emission from liquid cloud water, as these can dominate the measured Tb, especially at high frequencies, leaving little information about the surface.

C. Optimal Estimation Retrieval Information Content

Ignoring errors in T_s , the degree to which the estimated emissivity is determined by observations (rather than the prior) can be assessed by examining the posterior error covariance matrix

$$\mathbf{S}_x = (\mathbf{S}_a^{-1} + \mathbf{K}^T \mathbf{S}_y^{-1} \mathbf{K})^{-1} \quad (3)$$

and averaging kernel

$$\mathbf{A} = \mathbf{S}_x (\mathbf{K}^T \mathbf{S}_y^{-1} \mathbf{K}). \quad (4)$$

Both of these terms are driven by the sensitivity of the observation brightness temperatures to the emissivity in the Jacobian matrix \mathbf{K} . This is strongly related to the optical depth of the atmosphere, which at GMI frequencies under cloud- and precipitation-free conditions corresponds to the column water vapor (CWV). In the limiting case of an optically thin atmosphere, and ignoring off-diagonal terms (because we assume independent emissivities at each channel), K_{ii} are approximately equal to T_s , and then $S_{x,ii}$ become $T_s^2 S_{y,ii}^{-1}$. This term is much larger than $S_{a,ii}^{-1}$, and thus $S_{x,ii}$ can be approximated as $S_{y,ii} T_s^{-2}$, and A_{ii} are close to one. In Figure 3, A_{ii} , the averaging kernel for emissivities, is shown as a function of CWV. We note that at 89 GHz and below, the condition of A_{ii} close to one is satisfied for most CWV values, although the information content at 89 GHz does decrease slightly over the terrestrial range of CWV. At 166 GHz, the sensitivity of brightness temperature to emissivity decreases rapidly with increasing CWV, causing a corresponding decrease in the averaging kernel diagonals and increase in \mathbf{S}_x which asymptotically approach the prior values (\mathbf{S}_a) at about 40 mm of CWV.

D. DPR matching and Cloud/Precipitation Screening

The emissivity retrievals, which are performed for each set of co-registered GMI brightness temperatures, are nearest-neighbor mapped to the DPR coordinate system, which consists of 49 cross-track pixels per scan over a 245km swath and approximately 7930 scans per orbit, with a nominal

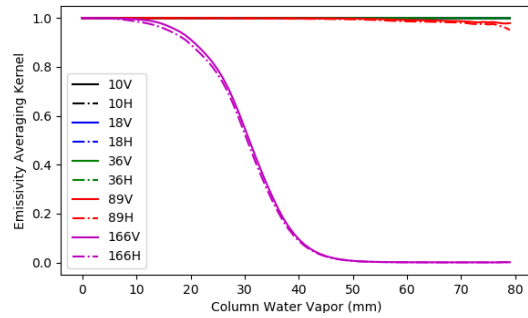


Fig. 3. Mean diagonal elements of the retrieved emissivity averaging kernel as a function of column water vapor.

ground footprint of 5km per pixel [34]. Fields from DPR Level 2 products are used to facilitate further screening and categorization of the emissivity- σ_0 database; these include the Ku and Ka data quality flags, GANAL skin temperature (for bias correction of emissivities for applications that use the GANAL inputs), precipitation flag, σ_0 saturation flags, land surface type, snow/ice cover flag, and vertically integrated precipitation water content.

Three datasets are used to remove cloud- and precipitation-affected pixels from the matched emissivity- σ_0 dataset: the retrieval normalized error, Φ_N , the DPR precipitation flag, and the MERRA-2 CLWP. The retrieval normalized error is adapted from (1) as

$$\Phi_N = \frac{\Phi}{n_{\text{obs}} + n_{\text{var}}}, \quad (5)$$

and large values indicate a large departure from the background state and/or inability of the forward model to replicate the observations. The most common reason for a large value of Φ_N is hydrometeor scattering, which produces brightness temperatures in the S2 channels that are too cold to be replicated with any realistic combination of surface emissivity and water vapor. However, because the scattering signal can be masked by emission from cloud liquid water and water vapor, particularly for shallow clouds, the DPR precipitation flag is also used to screen out precipitation-affected pixels. Figure 4 shows that the fraction of pixels with precipitation detected by DPR increases rapidly with $\Phi_N \geq 0.5$.

The matched GPM-CloudSat dataset [62] was also used to verify this threshold for precipitation, given the much greater sensitivity of CloudSat to light precipitation while acknowledging that the matchups are subject to some co-location error due to timing differences and differences in the sensor footprint, as well as spatial representativeness (the CloudSat-GPM matchups are biased towards high latitudes). Nevertheless we note generally good agreement with the DPR detection as a function of Φ_N for rainfall but a slightly lower threshold for falling snow, around $\Phi_N \geq 0.3$. There is also a substantial fraction (about 10%) of pixels with $\Phi_N < 0.3$ that are still classified as snow certain or probable by CloudSat, but are not able to be detected by the Φ_N screening method. It is possible that these events are shallow enough to be masked by water vapor and/or liquid cloud emission above the scattering hydrometeors, or simply do not consist of a large enough ice water path to produce a detectable scattering depression at the GMI frequencies.

In order to determine the appropriate threshold on CLWP, we examine the impact of unaccounted cloud water on the retrieved emissivities in Figure 5. The error in retrieved emissivity depends on both the true emissivity as well as the CLWP. The largest errors are for the combination of low true emissivity and large CLWP. Small negative error can exist at higher frequencies when the true emissivity is close to one, because the cloud becomes opaque and emits at a lower temperature than the surface. A CLWP as low as 0.02 kg m^{-2} can introduce significant error (relative to that from uncertainties in the atmospheric profile; see Figure 3a) at 89 and 166 GHz with emissivities < 0.75 , whereas a CLWP of 0.1 kg m^{-2} is not problematic at lower frequencies and/or emissivities > 0.85 . The fraction of observations with CLWP exceeding these thresholds is shown in Figure 4 as a function of Φ_N . It is notable that a significant fraction of observations exceed both thresholds at Φ_N values far below those associated with precipitation, justifying the use of a CLWP screen. It is also notable that Φ_N steadily increases with the fraction of observations containing CLWP, suggesting that there is some

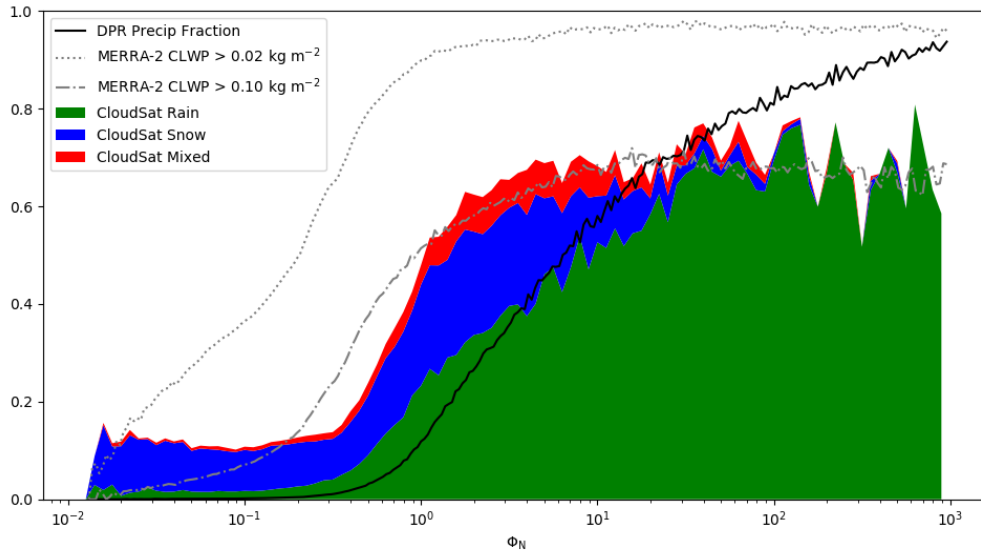


Fig. 4. Probability of precipitation (from the DPR precipitation flag), probability of precipitation from CloudSat (profiles flagged as certain, probable, or possible in each precipitation phase), and mean MERRA-2 cloud liquid water path as a function of residual normalized error. Data were compiled from all CloudSat-GPM matchups between March 2014 and December 2018 over land surfaces.

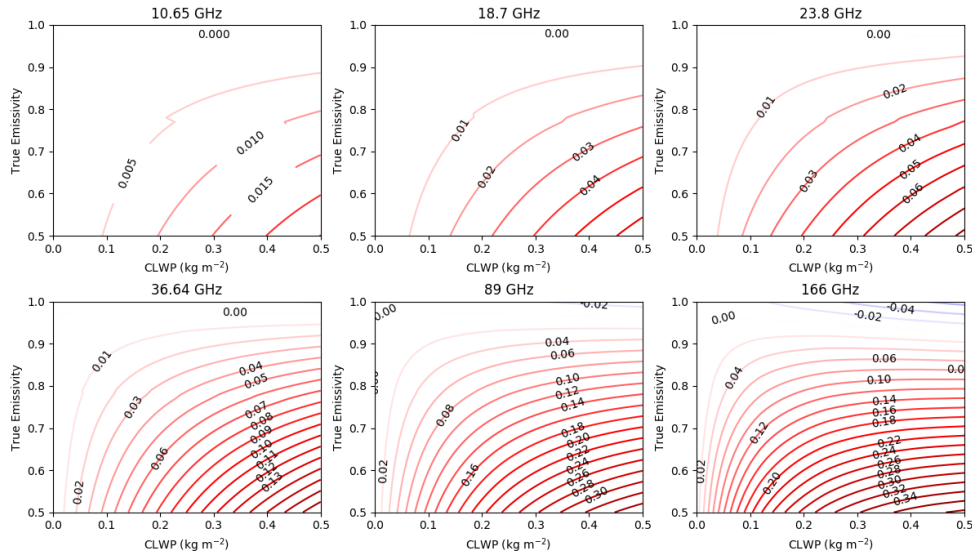
information in the microwave radiances related to the presence of cloud liquid water over land as suggested by [63], [64], and [65]. With stronger constraints on the surface emissivity our retrieval technique could conceivably retrieve CLWP over some land surfaces.

Considering that the Φ_N threshold of detection for snow is slightly lower than for rain and that low-emissivity surfaces are more prone to CLWP-induced error than high-emissivity surfaces, and balancing the desire for uncontaminated estimates with the need for sufficient samples to derive means and covariances on fine spatial scales, we chose to set different thresholds based upon DPR snow-IceCover flag for compilation of uncontaminated emissivity estimates and σ_0 observations for the classification in section III:

- For snow-covered surfaces and sea ice: no DPR-detected precipitation, $\Phi_N \leq 0.3$, and $\text{CLWP} \leq 0.02 \text{ kg m}^{-2}$;
- For all other surfaces: no DPR-detected precipitation, $\Phi_N \leq 0.5$, and $\text{CLWP} \leq 0.1 \text{ kg m}^{-2}$.

To demonstrate the importance of the CLWP screening step, the difference in average emissivity at 89 GHz H-pol between observations that have only been filtered to exclude precipitation (DPR precipitation flag and Φ_N threshold), and those filtered with both precipitation and CLWP thresholds, is shown in Figure 6. Note the regions with a high percentage of observations that do not pass the cloud screening test despite passing the precipitation-screening tests in Figures 6a and 6b. When these regions are coincident with a low background emissivity, such as eastern Canada and Russia in January, Antarctic sea ice, and coastal regions, the precipitation-cleared emissivity is biased high relative to the cloud- and precipitation-cleared scenes, consistent with the error analysis in Figure 5. When these cloudy-but-not-precipitating regions are coincident with high background emissivity, as is the case in the equatorial rainforests, a small negative bias in the retrieved emissivity is noted, again consistent with Figure 5.

As a final step in preparation for classification, the DPR-resolution orbital data that pass the pre-



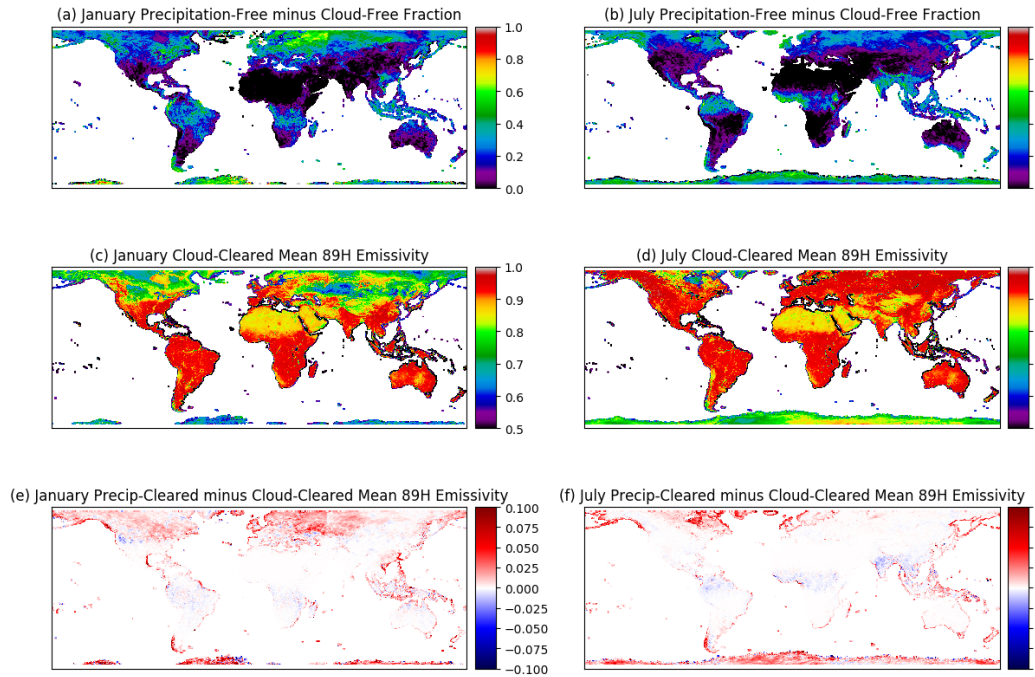


Fig. 6. Fraction of retrievals that pass the DPR precipitation flag and Φ_N precipitation-screening tests, but not the cloud liquid water screening test for (a) January and (b) July. Mean cloud- and precipitation-cleared emissivity at 89H in (c) January and (d) July. Difference between precipitation-cleared and cloud-cleared mean 89H emissivity in (e) January and (f) July.

angle ranges from 0° - 2° , 2° - 4° and 6° - 8° for both Ku and Ka, in addition to 10° - 12° and 14° - 16° for Ku. With passive and active observations having different amplitudes of variability and different units, the inputs are normalized by their variance over the entire dataset. Three separate classifications are performed: one for snow-free surfaces; another for snow-covered surfaces; and another for sea ice. These categories are obtained from the DPR snow/ice cover flag, which is derived from the Interactive Multisensor Snow and Ice Mapping System (IMS) product [67]. For the classifications, clusters are identified that describe self-similar surfaces in the multi-dimensional space spanning the passive and active microwave characteristics. Each cluster is characterized by the coordinates of its center in this space. The classification is performed on the monthly gridded means, allowing for a change in cluster at a given location in different months.

However, the cluster center coordinates are derived only once using the entire 12-month dataset, so the definition of each cluster does not change from month to month.

B. The snow-free surface clusters

In order to have enough clusters to represent the variability of soil and vegetation and at the same time to limit the number of clusters for the analysis, a number of 20 clusters is chosen. Note that there are eight passive microwave variables as well as eight active parameters (coming from the different frequencies and incidence angle bins) used for the classification, giving the same weight to the passive and active modes.

Figure 7 presents the meaningful maps obtained for the snow-free classification results for January and July. They show well-known geographical features and for example, some vegetation types clearly

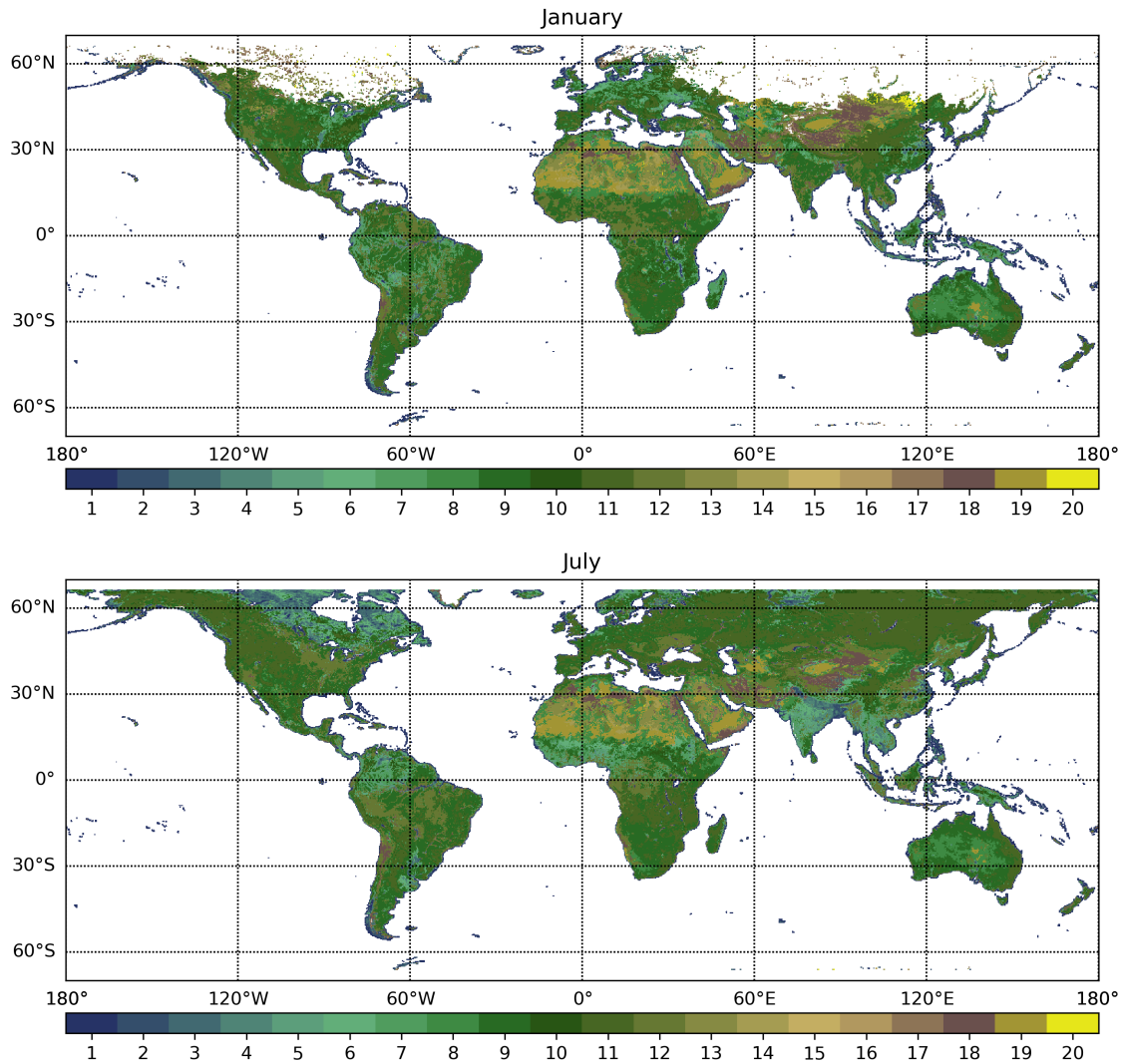


Fig. 7. Snow-free surface classification for January (top) and July (bottom).

stand out, such as the deserts or the rain forests. Figure 8 represents the center of each cluster for all passive and active parameters and a histogram of cluster area averaged over the annual cycle.

Clusters 1 to 4 are coastal areas and wetlands with relatively low leaf area index. They include the floodplains of the Amazon, the Mississippi, and the Congo rivers. These surfaces are characterized by low emissivities (V-pol channels <0.8 and H-

pol channels <0.7) and large differences between polarizations. The backscattering at nadir is high. Comparing January and July, notice the change in cluster over India to a more wetland-like cluster during the monsoon. This is visible to a lesser extent over the Sahel and Orinoco in Venezuela.

Clusters 5 to 11 indicate increasing vegetation density, with decreasing polarization difference in the emissivity and decreasing backscattering (as

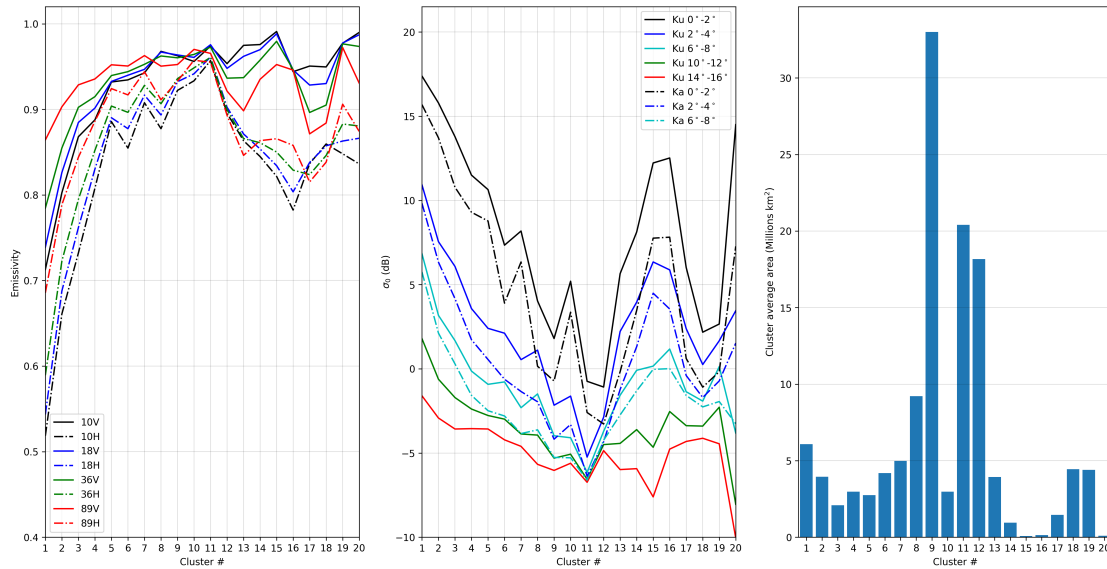


Fig. 8. Centre of each cluster for the snow-free surface classification for each passive and active microwave inputs (the emissivity is unitless and the normalized surface backscatter cross-section is in dB).

also observed in [68]). Clusters 7 to 11 correspond to very densely vegetated areas with a very low polarization difference and low backscattering: they are representative of evergreen broadleaf forest and mixed forest according to the IGBP land cover [69]. Cluster 8 also includes some surfaces with little vegetation, but similar roughness characteristics at the microwave wavelengths. Clusters 12 to 14 correspond to decreasing vegetation, with increasing emissivity polarization differences, high emissivity at vertical polarization, and increasing backscattering at low incidence angles. Sand deserts correspond to clusters from 15 to 20, with low emissivity at horizontal polarization and very high polarization difference [51], [70]. Some coastal areas are also included in clusters 17 and 18, which are primarily focused on carbonate outcrops in Yemen and center Asia. Water and carbonate surfaces have very similar microwave radiometric signatures, as already mentioned in different studies [70], [71], and confirmed here even when adding GPM DPR backscatter observations in the analysis.

Figure 9 shows examples of the absolute value

of the covariance matrices for clusters 2, 6, 11, and 19, representative respectively of coasts, wetlands, dense vegetation and sand deserts. Figure 9 shows that there is a great variability of covariances between channels and between emissivity and backscatter from a cluster to another. For the coastal cluster, channels of a similar footprint size (e.g., 10 GHz, 19-36 GHz) are strongly correlated, since the fraction of land within the footprint is the driving factor for emissivity. The backscatter and emissivity have a strong inverse correlation for the same reason, except at 166V where the land and ocean emissivity are similar. Wetlands (cluster 6) share similar behavior although the footprint size is less important owing perhaps to more homogeneous conditions within this cluster, and the emissivity-backscatter correlations are weaker than for the coastal cluster. Dense vegetation (cluster 11) shows positive correlations among all channels that decreases with increasing frequency difference (polarization is less important because the polarization difference is minimal for this cluster). However, the H-pol channels are more strongly

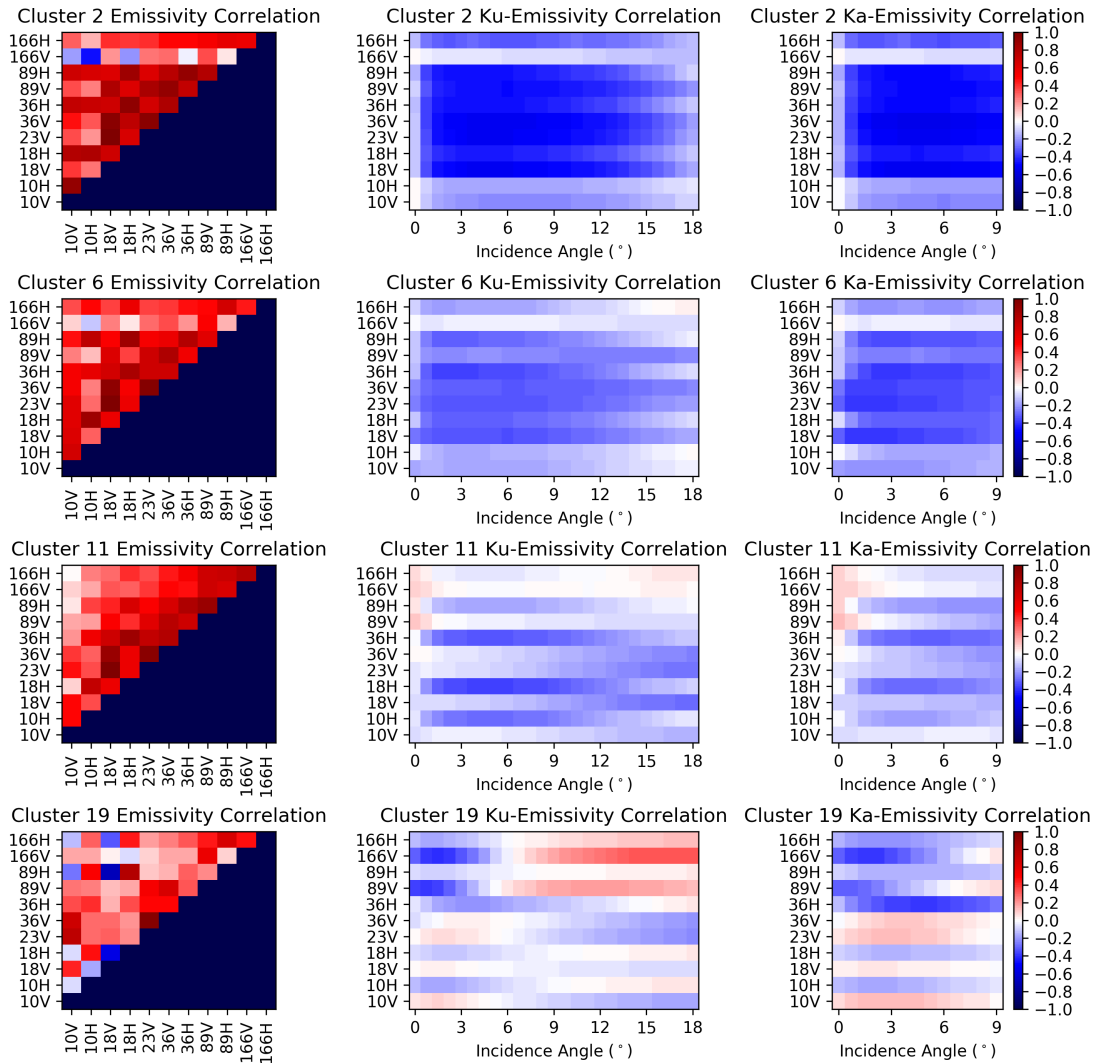


Fig. 9. Correlation matrix for emissivity and emissivity-backscatter relationships for selected snow-free surfaces representing coasts (2), wetlands(6), dense vegetation (11), and sandy deserts (19).

correlated to backscatter than the V-pol channels, and most prominently at frequencies similar to the radar frequency, indicating that variations in surface roughness on the scale of the radar wavelength are the dominant factor for emissivity-backscatter covariability in this cluster. Finally, over the sandy deserts (cluster 19), emissivity correlation rapidly drops off with frequency difference. This is likely due to the frequency-dependent penetration depth

that alters the effective surface temperature, and the non-linearity in scattering efficiency of sand grains with frequency (Raleigh scattering approximation). Backscatter-emissivity correlations are strongest at the vertically-polarized high frequencies (89 & 166 GHz), which have the shallowest penetration depth (compared to lower frequencies and horizontal polarizations) and thus are more influenced by surface characteristics than the subsurface temperature

profile. The correlations change sign as a function of incidence angle, indicating some competition between roughness and dielectric variability.

C. The snow-covered surface clusters

A classification of the snow-covered surfaces is also conducted. It only considers pixels flagged as snow by the DPR snowIceCover flag. For the snow classification, the 166 GHz emissivities for both vertical and horizontal polarizations have been added, as previous analyses showed that high frequencies are very sensitive to snow presence and surface properties (e.g., [72], [73]). To emphasize more the influence of higher frequencies in the classification, weights are doubled in the 89 GHz and 166 GHz bands. Figure 10 presents the classification of the snow-covered surfaces in the northern hemisphere, for three months (Nov., Jan., and Mar.). Significant changes are observed in the snow classification maps, illustrating the strong temporal variability of the snow responses through the season as already observed with passive and active observations by [74].

Figure 11 shows the centers of each cluster for each considered parameter. Clusters 1 and 2 represent ice sheets. Greenland mostly belongs to these clusters. Clusters 3 to 10 correspond to cold and dry snow. The emissivities at high frequencies are very low due to strong scattering in the snow whereas the low frequencies show rather high emissivities, which may be a consequence of the combination of deep penetration depth and insulating properties of these snowpacks. Backscattering at all angles tends to decrease with emissivity in these clusters. These clusters correspond to cold and dry snow like tundra or taiga (Eastern Siberia and Northern America) [75]. Clusters 10 to 14 have increasing emissivities and low backscattering for all frequencies and angles. They are related to mountain or maritime snow, with high emissivities even at high frequencies. These clusters correspond to mountain and prairie snow in the Sturm classification. For clusters 15 to 20, the emissivities again decrease at the high frequencies and backscatter increases, especially near nadir. On the maps, these clusters

are dominant in the early season and at lower latitudes, indicating that they likely represent relatively shallow, ephemeral snowpacks.

Figure 12 presents the emissivity and emissivity-backscatter correlation matrices for three clusters representing ice sheets (1), deep dry snowpacks over tundra (5), and seasonal snow over vegetated surfaces (15). The 10-36 GHz emissivities over the ice sheets have a strong correlation among each other and are decoupled from the 89 and 166 GHz emissivities. The backscatter at Ku band is negatively correlated to emissivity at 10-36 GHz, with increasing (decreasing) magnitude of the correlation with increasing incidence angle at horizontal (vertical) polarization. Ka-band backscatter shows a similar pattern with the strongest correlations shifted to higher frequencies (18-89 GHz). The deep snowpacks (cluster 5) present quite a different emissivity correlation matrix, with the 10 GHz channels decoupled from all higher frequencies. The emissivity-backscatter correlations are quite strong, especially at Ka band, and at frequencies ≥ 36 GHz show a pattern with weak positive correlations near nadir and strong negative correlations off nadir, consistent with increasingly specular reflecting surface with increasing snow depth. These patterns are similar for the shallow snow over vegetated surfaces (cluster 15), except that the 10 GHz channels are even more poorly correlated to the other emissivities and backscatter, an indication that the snow is not often deep enough to affect the 10 GHz emissivity.

D. The sea ice clusters

An additional classification is performed for surfaces identified as sea or lake ice, that is, water surfaces that have ice cover as indicated by the DPR snowIceCover flag. The same inputs as for the snow classification are used, but due to the fewer degrees of freedom for sea ice than for snow-free and snow-covered land, only a number of 10 clusters is chosen. Figure 13 shows maps of the clusters for the month of maximum sea ice extent in each hemisphere (March and September), keeping in mind the limit of the GPM orbit to $\pm 65^\circ$.

Figure 14 shows the centers of each cluster for each considered parameter. Cluster 1 represents the

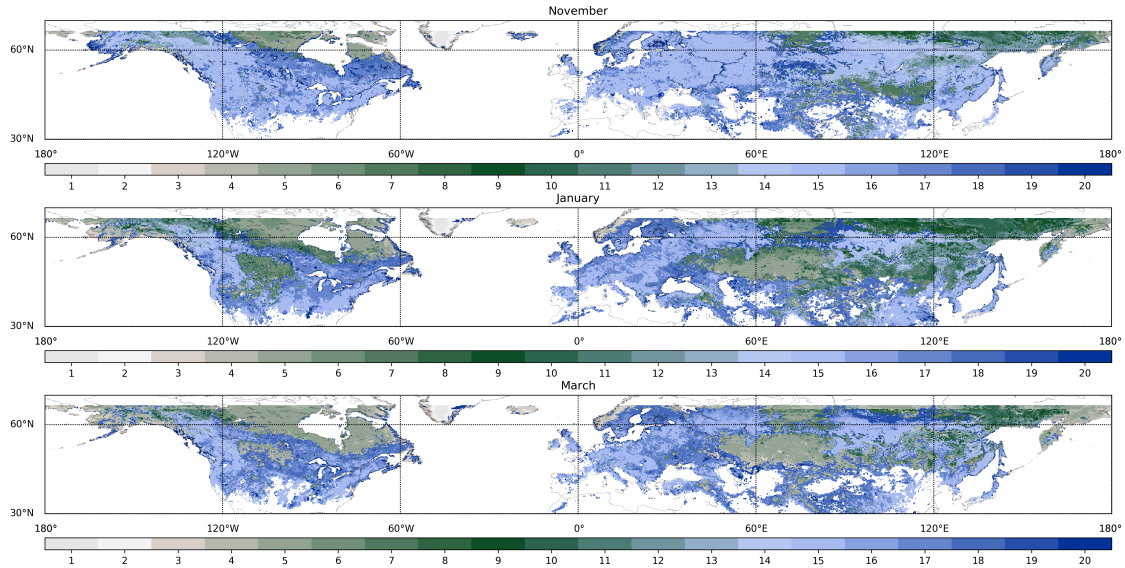


Fig. 10. Northern Hemisphere snow-covered surface classification for November (top), January (middle), and March (bottom).

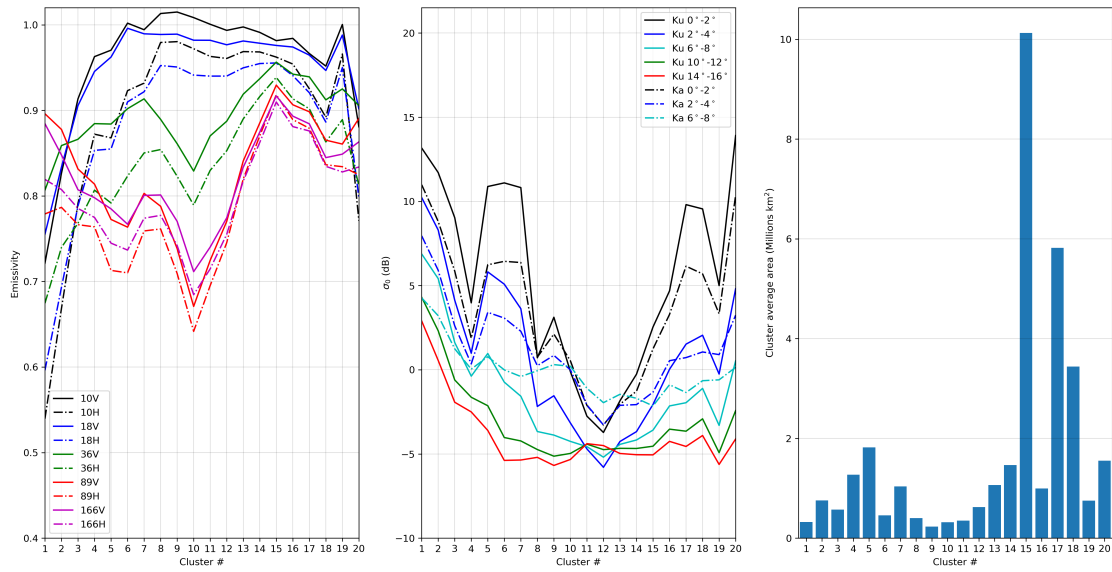


Fig. 11. Center of each cluster for the snow-covered surface classification, for each passive (left) and active (center) inputs. The spatial extent of each cluster is shown on the right panel.

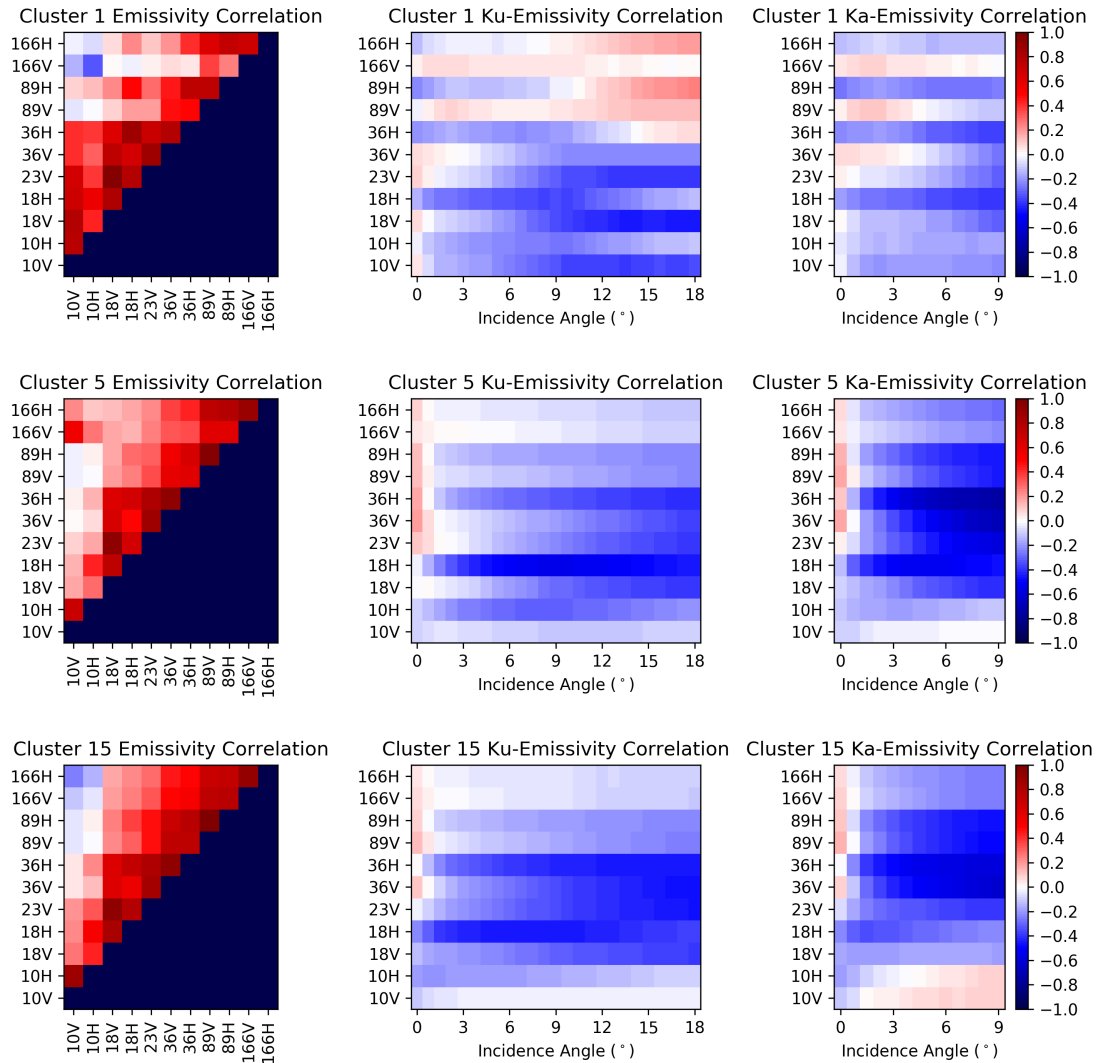


Fig. 12. Correlation matrix for emissivity and emissivity-backscatter relationships for selected snow-covered surfaces representing ice sheets (1), deep dry snow (5), and shallow snow (15).

marginal ice zone, then there is a trend towards increasing emissivity (especially at horizontal polarization) and decreasing off-nadir backscatter from clusters 2-7, representing increasing concentrations of sea ice. These trends are reversed from clusters 8-10, but with weaker polarization differences. These clusters are common during melting season, so perhaps they represent sea ice with melt ponds (which can contribute to high near-nadir backscatter) and

wet snow cover.

Figure 15 presents the correlation matrices for clusters 2 (low concentration sea ice), 7 (high concentration sea ice), and 10 (sea ice with melt ponds). Note that there is a high degree of similarity in the covariance matrices between emissivities, partially due to the monthly classification grid which may not represent changing sea ice concentrations within a month or anomalies within a particular year, thereby

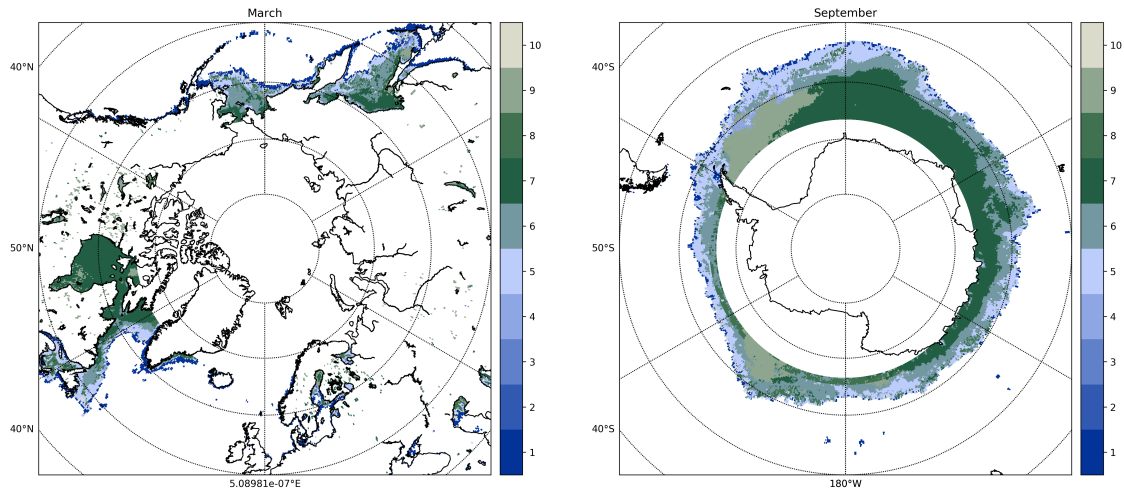


Fig. 13. Sea ice classification for the Northern Hemisphere in March (left) and Southern Hemisphere in September (right).

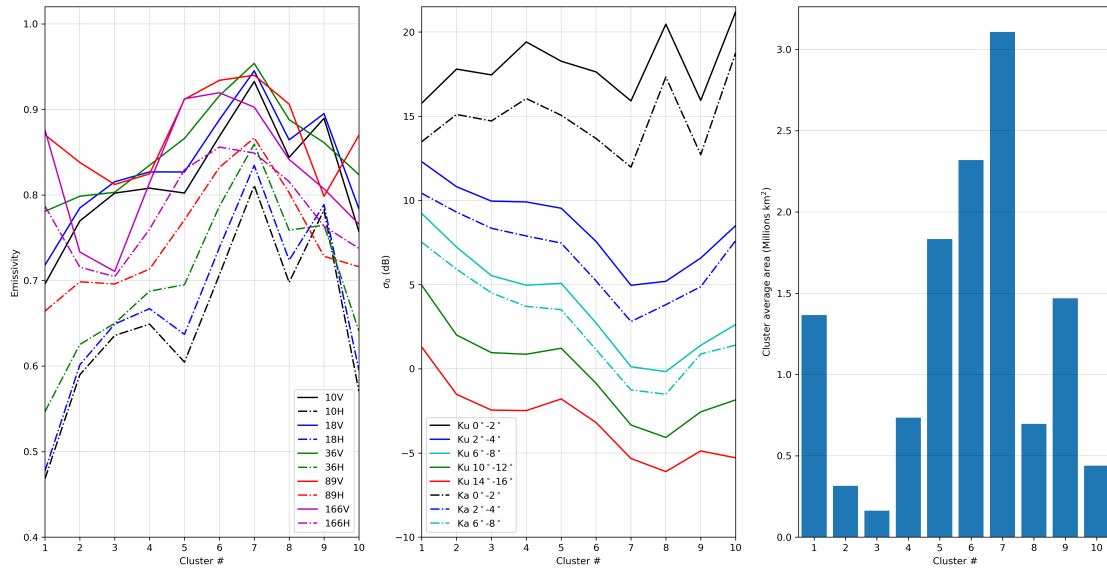


Fig. 14. Center of each cluster for the sea ice classification, for each passive (left) and active (center) inputs. The spatial extent of each cluster is shown on the right panel.

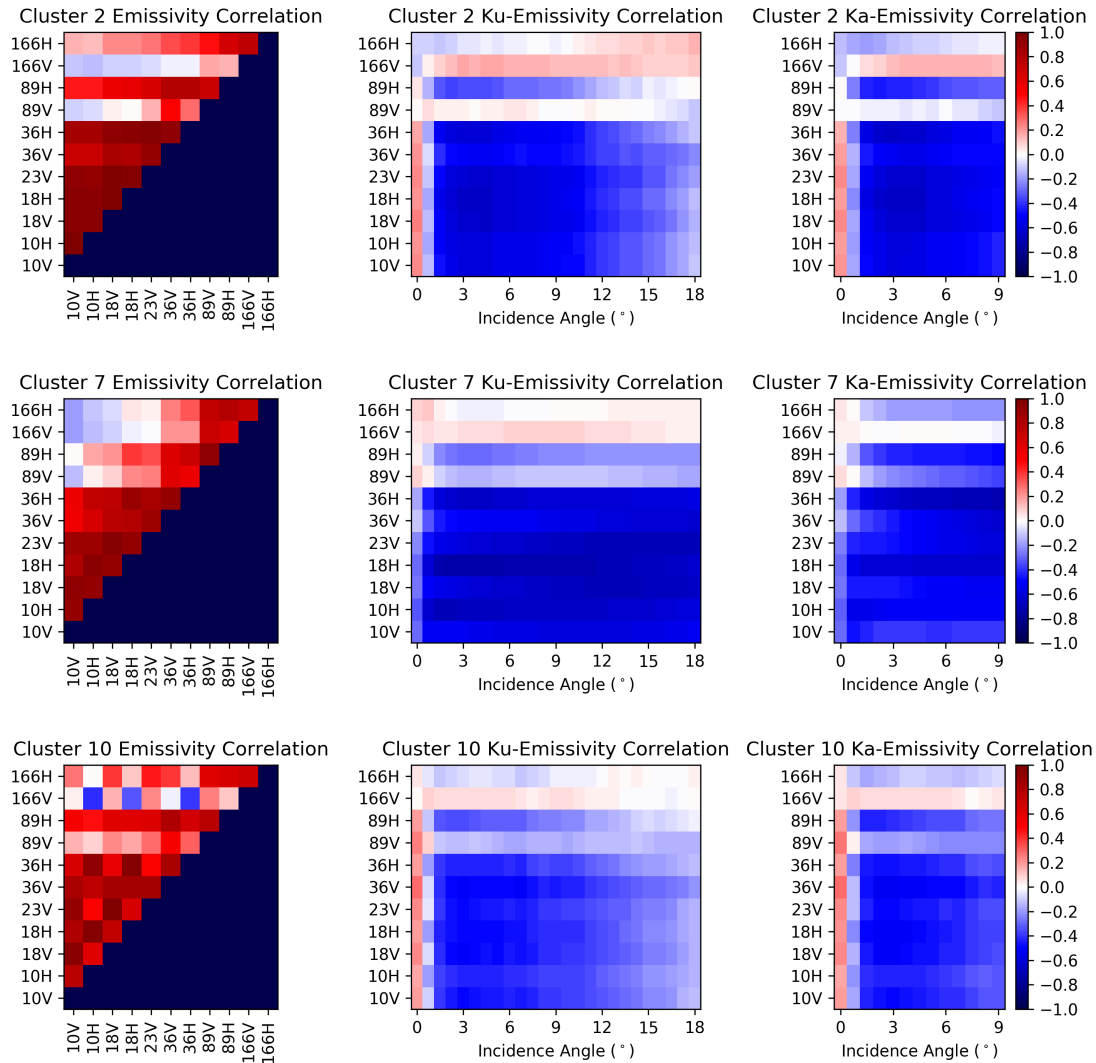


Fig. 15. Correlation matrix for emissivity and emissivity-backscatter relationships for selected sea ice clusters representing low concentration (2), high concentration (7), and melt ponds (10).

allowing several classes of sea ice to contribute to the covariance calculations. Nevertheless some differences are worth noting, in particular, in class 2 the 89V and 166V emissivities are decoupled from the other channels whereas in class 7 there are strong correlations between nearby frequencies and class 10 displays strong anticorrelation between 166V and the other H-pol channels. Like snow classes 5 and 15, there is a weak positive correlation

between nadir backscatter and emissivity but this shifts to a strong negative correlation at off-nadir angles. Much of this behavior is consistent with the effect of replacing a relatively low-emissivity, rough water surface with higher-emissivity sea ice, less rough (which acts to reduce off-nadir backscatter) sea ice, so the primary factor in these relationships is sea ice concentration.

IV. APPLICATIONS

In this section we document the use of the active-passive surface database and classification in the GPM Level 2 precipitation retrieval algorithms (in particular, the combined radar-radiometer algorithm and radiometer-only Goddard Profiling Algorithm GPROF). We also demonstrate the use of the data for investigations of the surface emissivity response to rain and snowfall.

A. Implementation in GPM Precipitation Retrieval Algorithms

The properties of the earth's surface are important for the combined algorithm in two ways: The normalized radar backscatter cross-section, σ_0 , is needed for deriving estimates of the path-integrated attenuation (PIA) which is an observational input to the ensemble filter method at the core of the combined algorithm retrieval [37], and the surface emissivity is necessary to simulate the brightness temperatures that are used in the filter as well. Since emissivity and reflectivity are inversely related by Kirchoff's law of thermal radiation, and σ_0 is a measure of a surface reflectivity at a particular angle, it is advantageous to use relationships between emissivity and σ_0 to further constrain the ensemble than if no relationship between emissivity and σ_0 was assumed. For water surfaces, a geophysical model function is used for emissivity and σ_0 [76], whereas land and sea ice follow a statistical treatment.

Over land and sea ice, surfaces are considered to belong to distinct clusters (derived in Section III) describing different levels of vegetation and snow cover, sea ice, wetlands, and coasts. In each of these clusters, an emissivity- σ_0 covariance matrix has been derived from precipitation-free observations. The empirical orthogonal functions (EOFs) of emissivity and σ_0 are then used to create ensembles of perturbed emissivity- σ_0 values that follow the observed correlation structure by assigning each EOF a random normally distributed value:

$$\epsilon_k(f, p) = \bar{\epsilon}(x, y, t, f, p) + \sum_{i=1}^{N_{EOF}} r_{k,i} E_i(s, f, p), \quad (6)$$

and

$$\sigma_{0,k}(f, \theta) = \sigma_{0,ref} + \sum_{i=1}^{N_{EOF}} r_{k,i} E_i(s, f, \theta) - PIA(k, f), \quad (7)$$

where ϵ_k is the emissivity in the k^{th} ensemble member at frequency f and polarization p , $\bar{\epsilon}$ is the mean emissivity at latitude x , longitude y , month t , frequency f , and polarization p , r is a random normally-distributed number with a mean of zero and standard deviation of one, and E is the magnitude of the i^{th} EOF for surface class s , frequency f , and polarization p . A similar procedure is followed to derive σ_0 for each ensemble member except that an incidence angle (θ) dependency is added and the reference value $\sigma_{0,ref}$ comes directly from the 2ADPR product, which uses a hybrid reference method to optimally combine spatial, temporal, and dual-frequency precipitation-free reference values. In this way, for example, the corresponding increase in σ_0 and decrease in emissivity that occurs with increasing soil moisture over some surfaces may be replicated in the ensemble filter framework.

The retrieved emissivities described in this manuscript have also been implemented operationally into the passive microwave precipitation algorithm for the GPM constellation sensors. This is done via the Goddard Profiling Algorithm (GPROF), within the forward modeling component creating the retrieval database from combined algorithm output, as described in [35]. Specifically, the retrieved emissivities are used in computing the surface emission component of brightness temperature, which for land areas and clear skies form the bulk of the top of the atmosphere signal at the lower microwave frequencies.

B. Emissivity response to the previous rainfall events

Studies showed that the clear-sky emissivity, especially at the low frequencies (e.g., 10 and 19 GHz) may be able to memorize the previous rainfall events information. For example, [38] noticed that the emissivity at 19H has a noticeable decrease after previous one-day rainfall accumulation greater than ~ 5 mm over the Southern Great Plains (SGP) site

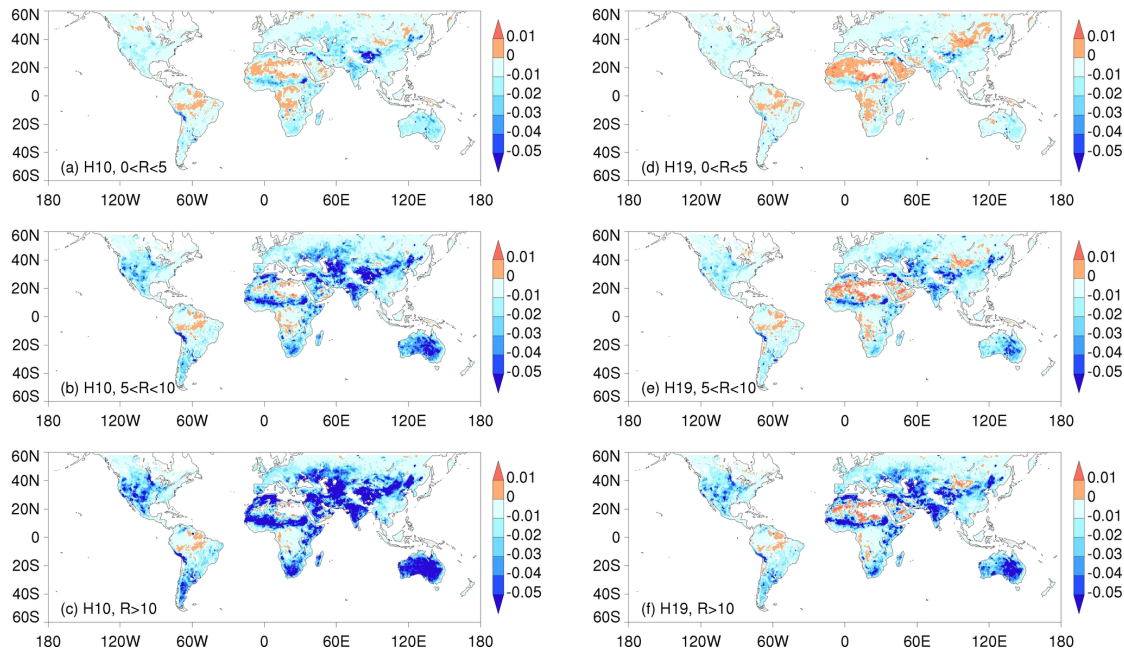


Fig. 16. First column: emissivity at H10, wet (rainfall occurs in previous one day) minus dry (no rainfall in previous one day) conditions. The rainfall accumulation (R) in previous one day is separated into three categories ($0 < R < 5$, $5 \leq R < 10$, $R \geq 10$). Second column: same as the first column except for H19.

(36.6°N, 97.5°W) in the United States. Figure 16 shows the emissivity response at 10H and 19H to the previous rainfall accumulation over the GPM covered land area. Specifically, we compute the emissivity differences at 0.25° resolution between wet (rainfall occurs in previous one day) and dry (no rainfall in previous one day) conditions. For the wet condition, the previous one-day rainfall accumulation (indicated by R) is further grouped into three categories, $0 < R < 5$, $5 \leq R < 10$, and $R \geq 10$ mm. The rainfall data is obtained from the Integrated Multi-Satellite Retrievals for GPM (IMERG) final run product at the half-hour and 0.1° resolution.

First, it is noticed that emissivity decreases over most of the land areas after rainfall events in the previous day, and the magnitude of the decrease corresponds to the rainfall amount, for both 10H and 19H. The emissivity drop is particularly evident with rainfall accumulation greater than 10 mm over Sahel, Southern Africa, Middle East, Indian sub-continent, northwest China, Australia continent, and

western United States (Fig. 16c and Fig. 16f). This apparent emissivity drop due to the previous rainfall impact therefore provides a potential means to estimate the rainfall accumulation. In fact, [77] showed that the retrieved rainfall accumulation by the emissivity drop over Southern Great Plains agrees reasonably well with the ground radar observations. These results suggest that the emissivity dataset described in this paper, along with applying the emissivity retrieval to other microwave sensors, could be used to estimate the rainfall accumulation over much of the GPM domain.

Second, it is noticed that there exist small positive emissivity responses to rainfall over several very densely vegetated regions (central Africa and Amazon), and very arid areas (Sahara Desert, Arabian Peninsula, and Taklamakan desert), which are more obvious when previous one day rainfall is < 5 mm (Fig. 16a, and Fig. 16d). The positive values mean that, on average, the emissivity associated with previous 1-day rainfall is higher than the emissivity

associated with no previous 1-day rainfall. This phenomenon directly contradicts the common behavior where rainfall causes emissivity to decrease. In arid regions, the penetration depth can be very large [52], and increases in moisture can decrease the penetration depth. Depending on season and time of the GPM overpass, this can result in an apparent increase in emissivity.

C. Emissivity response to snowfall

The surface emissivity and backscatter response to snow accumulation is complex, depending not only on snow water equivalent (SWE), but also on the density, grain size, liquid water content, and vertically layered structure [20], [22], [78]. For simplicity, only SWE is considered in this analysis and is obtained from the MERRA2 reanalysis, where surface snow properties are driven by precipitation and atmosphere via a three-layer snow model [79]. While this introduces model error (because SWE-sensitive observations are not directly assimilated) relative to direct SWE site measurements or more sophisticated regional datasets (e.g., SNODAS [80]) over large areas, over multiple seasonal cycles of GPM data it should be capable of illustrating general trends.

Using the 5-year, 0.25° gridded GMI emissivity-DPR backscatter database, we examine the change in emissivity and backscatter between observations associated with different levels of SWE in Figure 17. The emissivity and backscatter response varies depending on the underlying topography and vegetation. Croplands, such as the northern great plains of North America and the central Asian steppe, which tend to have little vegetation during the winter, show the strongest response (decrease in emissivity) to low levels of SWE ($< 10 \text{ kg m}^{-1}$) at 89 and 166 GHz. Some backscatter differences are also evident: near nadir, backscatter tends to decrease over boreal forests, whereas off-nadir, this reduction is limited to the Ob river basin in Western Siberia. Here, the changes with respect to SWE, especially at low frequencies, might be conflated with the surface signature of typical springtime flooding that is common in poleward-draining watersheds.

Comparing the $[1,10]$ and $[10,100] \text{ kg m}^{-1}$ SWE intervals (right panels of Figure 17, more pronounced responses are evident. Decreases in emissivity are evident at 18 GHz over prairies and dormant croplands; at 36-166 GHz they are evident everywhere at varying magnitudes. Near-nadir there is a decrease in backscatter over the tundra regions of Siberia and Canada. This can be explained by the reduction in Fresnel reflection from an air-dry snow interface relative to the air-ground interface. Off-nadir, the volume scattering component dominates [81], and the backscatter response inversely mirrors the emissivity response, particularly at Ka-band.

V. SUMMARY AND CONCLUSIONS

This manuscript presents an microwave emissivity retrieval method developed for the GPM Microwave Imager and applicable to any microwave sensor. It is applied to five years of GMI observations over snow-free and snow-covered land and sea ice. The emissivities are co-located with DPR surface backscatter measurements and screened for clouds and precipitation. The resulting database is used to provide an active-passive microwave characterization of surfaces within the GPM orbit for precipitation retrieval algorithms and other applications.

The emissivity retrieval method is novel in that the full emissivity vector is retrieved from 10-166 GHz using optimal estimation, and only weak a priori constraints are placed on individual channels with no assumed covariance. While appropriate for clear-sky radiative transfer, these assumptions can lead to contamination of retrieved emissivities with cloud and precipitation artifacts which has plagued previous studies [38]. Because GMI includes water vapor sounding channels, retrieval of the atmospheric state can be performed simultaneously with the surface. Using the MERRA2 reanalysis (which does not assimilate GMI observations) as the a priori atmospheric state and knowledge of the error structure of the MERRA2 atmospheric state variables, we are able to effectively screen for cloud- and precipitation-affected emissivity retrievals. Comparisons with co-located CloudSat data show that this GMI-based screen is able to

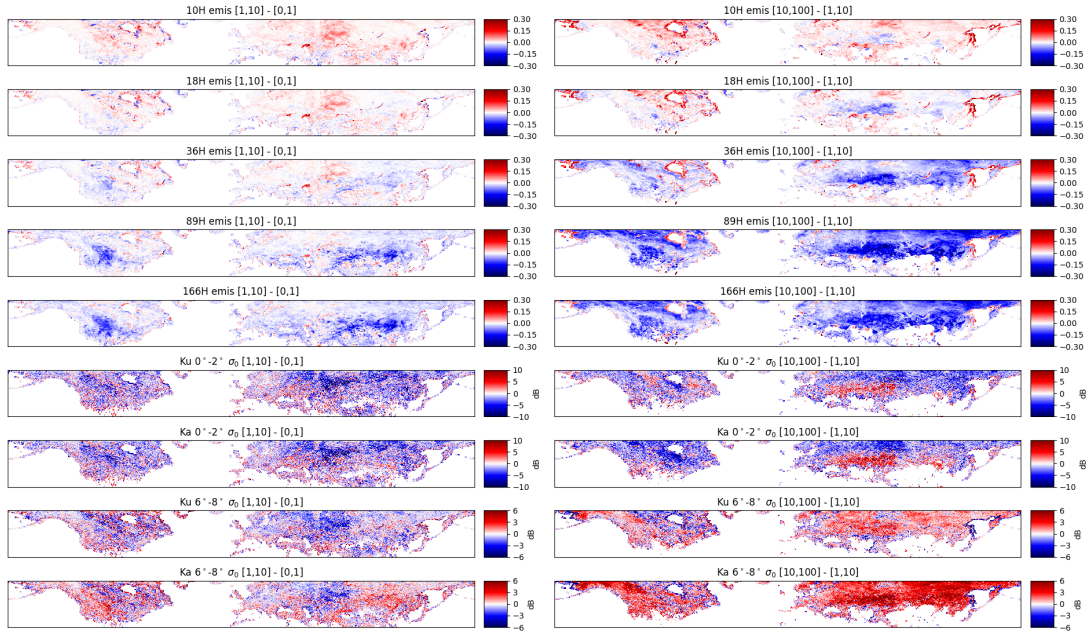


Fig. 17. Difference in emissivity at the horizontally polarized GMI channels and backscatter at Ku and Ka bands between 0° - 2° 6° - 8° incidence angles when MERRA2 SWE increases from $0 < \text{SWE} \leq 1 \text{ kg m}^{-2}$ to $1 < \text{SWE} \leq 10 \text{ kg m}^{-2}$ (left) and from $1 < \text{SWE} \leq 10 \text{ kg m}^{-2}$ to $10 < \text{SWE} \leq 100 \text{ kg m}^{-2}$ (right).

detect precipitation that DPR does not; however, about 10% of precipitation occurrence from Cloud-Sat (mainly light snow) is still undetectable by GMI, either because it produces too weak of a scattering depression or is shallow enough to be masked by emission from water vapor and/or liquid clouds.

The Kohonen classification technique was applied to monthly 0.25° gridded mean emissivities and backscatter distinctly for snow-free, snow-covered, and sea ice surfaces in order to identify self-similar surfaces within the bounds of the GPM orbit based on both active and passive microwave characteristics. In each case, the addition of active backscatter data provided some distinction between land surface types with similar emissivities; for example, coasts and carbonate outcrops. Snow and sea ice surfaces show clear seasonal cycles representing the asymmetric increase in dry snow/ice coverage and reduction via melting in the spring.

The surface classes have direct application in the GPM combined [37] and passive microwave [35]

precipitation retrieval algorithms. The combined algorithm uses the emissivity-backscatter covariance matrix for each class as a statistical model for the surface in its ensemble filter-based retrieval, while the passive algorithm showed improved agreement between observed and simulated database brightness temperatures when the retrieved emissivities described in our study are used in the database construction. Finally, we showcase potential applications of our database to develop retrievals of accumulated rain and snow using temporal differences in emissivity and backscatter. Strong signals for both exist over some surfaces; further development of methods to estimate these hydrological quantities from multi-satellite emissivity and backscatter measurements appears to be a promising avenue of future work.

ACKNOWLEDGMENT

The authors would like to thanks Dr. Wesley Berg of Colorado State University for providing

the atmospheric transmittance tables integrated over the GMI spectral response function. The authors would also like to thank Dr. Zeinab Takbiri at the University of Minnesota for providing the DPR-matched MERRA2 SWE values. This work was supported by NASA's Precipitation Measurement Missions Science team by Program Scientists Dr. Ramesh Kakar and Dr. Gail Skofronick-Jackson.

REFERENCES

- [1] T. Wilheit, R. Adler, S. Avery, E. Barrett, P. Bauer, W. Berg, A. Chang, J. Ferriday, N. Grody, S. Goodman *et al.*, "Algorithms for the retrieval of rainfall from passive microwave measurements," *Remote Sensing Reviews*, vol. 11, no. 1-4, pp. 163-194, 1994.
- [2] C. Kummerow, Y. Hong, W. Olson, S. Yang, R. Adler, J. McCollum, R. Ferraro, G. Petty, D.-B. Shin, and T. Wilheit, "The evolution of the goddard profiling algorithm (gprof) for rainfall estimation from passive microwave sensors," *Journal of Applied Meteorology*, vol. 40, no. 11, pp. 1801-1820, 2001.
- [3] K. Aonashi, J. Awaka, M. Hirose, T. Kozu, T. Kubota, G. Liu, S. Shige, S. Kida, S. Seto, N. Takahashi *et al.*, "Gsmap passive microwave precipitation retrieval algorithm: Algorithm description and validation," *Journal of the Meteorological Society of Japan. Ser. II*, vol. 87, pp. 119-136, 2009.
- [4] W. Bell, B. Candy, N. Atkinson, F. Hilton, N. Baker, N. Bormann, G. Kelly, M. Kazumori, W. F. Campbell, and S. D. Swadley, "The assimilation of ssmis radiances in numerical weather prediction models," *IEEE Transactions on Geoscience and Remote Sensing*, vol. 46, no. 4, pp. 884-900, 2008.
- [5] F. Karbou, F. Rabier, J.-P. Lafore, J.-L. Redelsperger, and O. Bock, "Global 4dvar assimilation and forecast experiments using amsu observations over land. part ii: Impacts of assimilating surface-sensitive channels on the african monsoon during amma," *Weather and Forecasting*, vol. 25, no. 1, pp. 20-36, 2010.
- [6] S.-A. Boukabara, K. Garrett, W. Chen, F. Iturbide-Sanchez, C. Grassotti, C. Kongoli, R. Chen, Q. Liu, B. Yan, F. Weng, R. Ferraro, T. Kleespies, and H. Meng, "MiRS: An All-Weather 1DVAR satellite data assimilation and retrieval system," *Geoscience and Remote Sensing, IEEE Transactions on*, vol. 49, no. 9, pp. 3249-3272, Sept 2011.
- [7] B. Yan and F. Weng, "Assimilation of f-16 special sensor microwave imager/sounder data in the ncep global forecast system," *Weather and Forecasting*, vol. 27, no. 3, pp. 700-714, 2012.
- [8] R. H. Reichle, D. B. McLaughlin, and D. Entekhabi, "Variational data assimilation of microwave radiobrightness observations for land surface hydrology applications," *IEEE Transactions on Geoscience and Remote Sensing*, vol. 39, no. 8, pp. 1708-1718, 2001.
- [9] C. D. Peters-Lidard, P. R. Houser, Y. Tian, S. V. Kumar, J. Geiger, S. Olden, L. Lighty, B. Doty, P. Dirmeyer, J. Adams *et al.*, "High-performance earth system modeling with nasa/gsf's land information system," *Innovations in Systems and Software Engineering*, vol. 3, no. 3, pp. 157-165, 2007.
- [10] K. Yang, T. Koike, I. Kaihotsu, and J. Qin, "Validation of a dual-pass microwave land data assimilation system for estimating surface soil moisture in semiarid regions," *Journal of Hydrometeorology*, vol. 10, no. 3, pp. 780-793, 2009.
- [11] X. Tian, Z. Xie, A. Dai, B. Jia, and C. Shi, "A microwave land data assimilation system: Scheme and preliminary evaluation over china," *Journal of Geophysical Research: Atmospheres*, vol. 115, no. D21, 2010.
- [12] R. Meneghini, T. Iguchi, T. Kozu, L. Liao, K. Okamoto, J. A. Jones, and J. Kwiatkowski, "Use of the surface reference technique for path attenuation estimates from the TRMM Precipitation Radar," *J. Appl. Meteor.*, vol. 39, pp. 2053-2070, 2000.
- [13] T. S. L'Ecuyer and G. L. Stephens, "An estimation-based precipitation retrieval algorithm for attenuating radars," *Journal of applied meteorology*, vol. 41, no. 3, pp. 272-285, 2002.
- [14] C. Mitrescu, T. L'Ecuyer, J. Haynes, S. Miller, and J. Turk, "Cloudsat precipitation profiling algorithm - model description," *J. Appl. Meteor. Climatol.*, vol. 49, pp. 991-1003, 2010.
- [15] Y. Kim, T. Jackson, R. Bindlish, H. Lee, and S. Hong, "Radar vegetation index for estimating the vegetation water content of rice and soybean," *IEEE Geoscience and Remote Sensing Letters*, vol. 9, no. 4, pp. 564-568, 2012.
- [16] F. T. Ulaby, P. P. Batlivala, and M. C. Dobson, "Microwave backscatter dependence on surface roughness, soil moisture, and soil texture: Part i-bare soil," *IEEE Transactions on Geoscience Electronics*, vol. 16, no. 4, pp. 286-295, 1978.
- [17] L. C. Smith, "Satellite remote sensing of river inundation area, stage, and discharge: A review," *Hydrological processes*, vol. 11, no. 10, pp. 1427-1439, 1997.
- [18] F. Weng, B. Yan, and N. C. Grody, "A microwave land emissivity model," *Journal of Geophysical Research: Atmospheres*, vol. 106, no. D17, pp. 20 115-20 123, 2001. [Online]. Available: <http://dx.doi.org/10.1029/2001JD900019>
- [19] H. Gao, E. F. Wood, M. Drusch, W. Crow, and T. J. Jackson, "Using a microwave emission model to estimate soil moisture from estar observations during sgp99," *Journal of Hydrometeorology*, vol. 5, no. 1, pp. 49-63, 2004.
- [20] C. Matzler and A. Wiesmann, "Extension of the microwave emission model of layered snowpacks to coarse-grained snow," *Remote Sensing of Environment*, vol. 70, no. 3, pp. 317 - 325, 1999. [Online]. Available: <http://www.sciencedirect.com/science/article/pii/S0034425799000474>
- [21] G. Picard, L. Brucker, A. Roy, F. Dupont, M. Fily, A. Royer, and C. Harlow, "Simulation of the microwave emission of multi-layered snowpacks using the dense media radiative transfer theory: the dmrt-ml model," *Geoscientific Model Development*, vol. 6, no. 4, pp. 1061-1078, 2013. [Online]. Available: <https://www.geosci-model-dev.net/6/1061/2013/>
- [22] G. Picard, M. Sandells, and H. Löwe, "Smrt: an active-passive microwave radiative transfer model for snow with multiple microstructure and scattering formulations (v1.0)," *Geoscientific Model Development*, vol. 11, no. 7, pp.

- 2763–2788, 2018. [Online]. Available: <https://www.geosci-model-dev.net/11/2763/2018/>
- [23] T. R. H. Holmes, M. Drusch, J. P. Wigneron, and R. A. M. de Jeu, "A global simulation of microwave emission: Error structures based on output from ecmwf's operational integrated forecast system," *IEEE Transactions on Geoscience and Remote Sensing*, vol. 46, no. 3, pp. 846–856, March 2008.
 - [24] L. Brucker, G. Picard, L. Arnaud, J.-M. Barnola, M. Schneebeli, H. Brunjail, E. Lefebvre, and M. Fily, "Modeling time series of microwave brightness temperature at dome c, antarctica, using vertically resolved snow temperature and microstructure measurements," *Journal of Glaciology*, vol. 57, no. 201, p. 171182, 2011.
 - [25] L. Brucker, A. Royer, G. Picard, A. Langlois, and M. Fily, "Hourly simulations of the microwave brightness temperature of seasonal snow in Quebec, Canada, using a coupled snow evolution-emission model," *Remote Sensing of Environment*, vol. 115, pp. 1966–1977, Aug. 2011.
 - [26] L. Brucker, G. Picard, and M. Fily, "Snow grain-size profiles deduced from microwave snow emissivities in antarctica," *Journal of Glaciology*, vol. 56, no. 197, p. 514526, 2010.
 - [27] F. J. Turk, L. Li, and Z. S. Haddad, "A physically based soil moisture and microwave emissivity data set for global precipitation measurement (gpm) applications," *IEEE Transactions on Geoscience and Remote Sensing*, vol. 52, no. 12, pp. 7637–7650, 2014.
 - [28] S. Ringerud, C. Kummerow, C. Peters-Lidard, Y. Tian, and K. Harrison, "A comparison of microwave window channel retrieved and forward-modeled emissivities over the us southern great plains," *IEEE Transactions on Geoscience and Remote Sensing*, vol. 52, no. 5, pp. 2395–2412, 2014.
 - [29] K. W. Harrison, Y. Tian, C. D. Peters-Lidard, S. Ringerud, and S. V. Kumar, "Calibration to improve forward model simulation of microwave emissivity at gpm frequencies over the us southern great plains," *IEEE Transactions on Geoscience and Remote Sensing*, vol. 54, no. 2, pp. 1103–1117, 2016.
 - [30] J. L. Bytheway and C. D. Kummerow, "A physically based screen for precipitation over complex surfaces using passive microwave observations," *IEEE Transactions on Geoscience and Remote Sensing*, vol. 48, no. 1, pp. 299–313, 2010.
 - [31] F. J. Turk, Z. S. Haddad, and Y. You, "Principal components of multifrequency microwave land surface emissivities. part i: Estimation under clear and precipitating conditions," *Journal of Hydrometeorology*, vol. 15, no. 1, pp. 3–19, 2014.
 - [32] F. Aires, C. Prigent, F. Bernardo, C. Jiménez, R. Saunders, and P. Brunel, "A tool to estimate land-surface emissivities at microwave frequencies (telsem) for use in numerical weather prediction," *Quarterly Journal of the Royal Meteorological Society*, vol. 137, no. 656, pp. 690–699, 2011.
 - [33] S. Durden, S. Tanelli, and R. Meneghini, "Using surface classification to improve surface reference technique performance over land," *92.60. Kc; 92.70. Bc; 84.40. Xb*, 2012.
 - [34] A. Y. Hou, R. K. Kakar, S. Neeck, A. A. Azarbarzin, C. D. Kummerow, M. Kojima, R. Oki, K. Nakamura, and T. Iguchi, "The Global Precipitation Measurement Mission," *Bull. Amer. Meteor. Soc.*, vol. 95, pp. 701–722, 2014.
 - [35] C. D. Kummerow, D. Randel, M. Kulie, N.-Y. Wang, R. Ferraro, S. J. Munchak, and V. Petkovic, "The evolution of the Goddard Profiling Algorithm to a fully parametric scheme," *J. Atmos. Oceanic Technol.*, p. accepted, 2015.
 - [36] S. Seto, T. Iguchi, and T. Oki, "The basic performance of a precipitation retrieval algorithm for the global precipitation measurement mission's single/dual-frequency radar measurements," *IEEE Transactions on Geoscience and Remote Sensing*, vol. 51, no. 12, pp. 5239–5251, 2013.
 - [37] M. Grecu, W. S. Olson, S. J. Munchak, S. Ringerud, L. Liao, Z. Haddad, B. L. Kelley, and S. F. McLaughlin, "The gpm combined algorithm," *Journal of Atmospheric and Oceanic Technology*, vol. 33, no. 10, pp. 2225–2245, 2016.
 - [38] R. R. Ferraro, C. D. Peters-Lidard, C. Hernandez, F. J. Turk, F. Aires, C. Prigent, X. Lin, S.-A. Boukabara, F. A. Furuzawa, K. Gopalan *et al.*, "An evaluation of microwave land surface emissivities over the continental united states to benefit gpm-era precipitation algorithms," *IEEE Transactions on Geoscience and Remote Sensing*, vol. 51, no. 1, pp. 378–398, 2013.
 - [39] C. D. Kummerow, S. Ringerud, J. Crook, D. Randel, and W. Berg, "An observationally generated a priori database for microwave rainfall retrievals," *Journal of Atmospheric and Oceanic Technology*, vol. 28, no. 2, pp. 113–130, 2011.
 - [40] C. Prigent, W. B. Rossow, and E. Matthews, "Microwave land surface emissivities estimated from ssm/i observations," *Journal of Geophysical Research: Atmospheres*, vol. 102, no. D18, pp. 21 867–21 890, 1997.
 - [41] C. Prigent, F. Aires, and W. B. Rossow, "Land surface microwave emissivities over the globe for a decade," *Bulletin of the American Meteorological Society*, vol. 87, no. 11, pp. 1573–1584, 2006.
 - [42] R. Meneghini, J. A. Jones, T. Iguchi, K. Okamoto, and J. Kwiatkowski, "A hybrid surface reference technique and its application to the TRMM Precipitation Radar," *J. Atmos. Oceanic Technol.*, vol. 21, pp. 1645–1658, 2004.
 - [43] R. Meneghini and J. A. Jones, "Standard deviation of spatially averaged surface cross section data from the trmm precipitation radar," *IEEE Geoscience and Remote Sensing Letters*, vol. 8, no. 2, pp. 293–297, 2011.
 - [44] F. J. Wentz and D. Draper, "On-orbit absolute calibration of the global precipitation measurement microwave imager," *Journal of Atmospheric and Oceanic Technology*, vol. 33, no. 7, pp. 1393–1412, 2016.
 - [45] W. Berg, S. Bilanow, R. Chen, S. Datta, D. Draper, H. Ebrahimi, S. Farrar, W. L. Jones, R. Kroodsma, D. McKague *et al.*, "Intercalibration of the gpm microwave radiometer constellation," *Journal of Atmospheric and Oceanic Technology*, vol. 33, no. 12, pp. 2639–2654, 2016.
 - [46] D. Draper, D. Newell, F. Wentz, S. Krimchansky, and G. Skofronick-Jackson, "The global precipitation measurement (GPM) microwave imager (GMI): Instrument overview and early on-orbit performance," *IEEE Journal of Selected Topics in Applied Earth Observations and Remote Sensing*, p. in review, 2015.
 - [47] G. W. Petty and R. Bennartz, "Field-of-view characteristics and resolution matching for the global precipitation mea-

- surement (gpm) microwave imager (gmi)," *Atmospheric Measurement Techniques*, vol. 10, no. 3, p. 745, 2017.
- [48] C. D. Rodgers, *Inverse methods for atmospheric sounding: theory and practice*. World scientific, 2000, vol. 2.
- [49] G. S. Elsaesser and C. D. Kummerow, "Toward a fully parametric retrieval of the nonraining parameters over the global oceans," *J. Appl. Meteor. Climatol.*, vol. 47, pp. 1599–1618, 2008.
- [50] D. I. Duncan and C. D. Kummerow, "A 1dvar retrieval applied to gmi: Algorithm description, validation, and sensitivities," *Journal of Geophysical Research: Atmospheres*, vol. 121, no. 12, pp. 7415–7429, 2016.
- [51] C. Prigent, W. B. Rossow, E. Matthews, and B. Marticorena, "Microwave radiometric signatures of different surface types in deserts," *Journal of Geophysical Research: Atmospheres*, vol. 104, no. D10, pp. 12 147–12 158, 1999.
- [52] H. Norouzi, W. B. Rossow, M. Temimi, C. Prigent, M. Azarderakhsh, S. Boukabara, and R. Khanbilvardi, "Using microwave brightness temperature diurnal cycle to improve emissivity retrievals over land," *Remote sensing of environment*, vol. 123, pp. 470–482, 2012.
- [53] R. Gelaro, W. McCarty, M. J. Suárez, R. Todling, A. Molod, L. Takacs, C. A. Randles, A. Darmenov, M. G. Bosilovich, R. Reichle *et al.*, "The modern-era retrospective analysis for research and applications, version 2 (merra-2)," *Journal of Climate*, vol. 30, no. 14, pp. 5419–5454, 2017.
- [54] Global Modeling and Assimilation Office (GMAO), "MERRA-2 inst3_3d_asm_Np: 3d, 3-Hourly, Instantaneous, Pressure-Level, Assimilation, Assimilated Meteorological Fields V5.12.4," accessed 5 February 2019, Greenbelt, MD, USA, 2015. [Online]. Available: 10.5067/QBZ6MG944HW0
- [55] —, "MERRA-2 inst1_2d_asm_Nx: 2d, 1-Hourly, Instantaneous, Single-Level, Assimilation, Single-Level Diagnostics V5.12.4," accessed 5 February 2019, Greenbelt, MD, USA, 2015. [Online]. Available: 10.5067/3Z173KIE2TPD
- [56] G. Moore, D. H. Bromwich, A. B. Wilson, I. Renfrew, and L. Bai, "Arctic system reanalysis improvements in topographically forced winds near greenland," *Quarterly Journal of the Royal Meteorological Society*, vol. 142, no. 698, pp. 2033–2045, 2016.
- [57] R. S. V. I. Durre and D. B. Wuerz, "Overview of the integrated global radiosonde archive," *Journal of Climate*, vol. 19, pp. 53–68, 2006.
- [58] S. Clough, M. Shephard, E. Mlawer, J. Delamere, M. Iacono, K. Cady-Pereira, S. Boukabara, and P. Brown, "Atmospheric radiative transfer modeling: a summary of the aer codes," *Journal of Quantitative Spectroscopy and Radiative Transfer*, vol. 91, no. 2, pp. 233–244, 2005.
- [59] F. Karbou and C. Prigent, "Calculation of microwave land surface emissivity from satellite observations: Validity of the specular approximation over snow-free surfaces?" *IEEE Geoscience and Remote Sensing Letters*, vol. 2, no. 3, pp. 311–314, 2005.
- [60] C. Matzler, "On the determination of surface emissivity from satellite observations," *IEEE Geoscience and remote sensing letters*, vol. 2, no. 2, pp. 160–163, 2005.
- [61] S. Guedj, F. Karbou, F. Rabier, and A. Bouchard, "Toward a better modeling of surface emissivity to improve amsu data assimilation over antarctica," *IEEE Transactions on Geoscience and Remote Sensing*, vol. 48, no. 4, pp. 1976–1985, April 2010.
- [62] J. Turk, "Cloudsat-gpm coincidence dataset (version 1c)," *NASA Technical Report*, 2016.
- [63] F. Aires, C. Prigent, W. Rossow, and M. Rothstein, "A new neural network approach including first guess for retrieval of atmospheric water vapor, cloud liquid water path, surface temperature, and emissivities over land from satellite microwave observations," *Journal of Geophysical Research: Atmospheres*, vol. 106, no. D14, pp. 14 887–14 907, 2001.
- [64] M. Deeter and J. Vivekanandan, "New dual-frequency microwave technique for retrieving liquid water path over land," *Journal of Geophysical Research: Atmospheres*, vol. 111, no. D15, 2006.
- [65] F. Aires, C. Prigent, S. A. Buehler, P. Eriksson, M. Milz, and S. Crewell, "Towards more realistic hypotheses for the information content analysis of cloudy/precipitating situations—application to a hyperspectral instrument in the microwave," *Quarterly Journal of the Royal Meteorological Society*, vol. 145, no. 718, pp. 1–14, 2019.
- [66] T. Kohonen, *Self-organization and associative memory*. Springer Science & Business Media, 2012, vol. 8.
- [67] S. R. Helfrich, D. McNamara, B. H. Ramsay, T. Baldwin, and T. Kasheta, "Enhancements to, and forthcoming developments in the interactive multisensor snow and ice mapping system (ims)," *Hydrological Processes: An International Journal*, vol. 21, no. 12, pp. 1576–1586, 2007.
- [68] C. Prigent, F. Aires, W. Rossow, and E. Matthews, "Joint characterization of vegetation by satellite observations from visible to microwave wavelengths: A sensitivity analysis," *Journal of Geophysical Research: Atmospheres*, vol. 106, no. D18, pp. 20 665–20 685, 2001.
- [69] M. Friedl, A. Strahler, J. Hodges, F. HALL, G. COLLATZ, B. MEESON, S. LOS, E. BROWN DE COLSTOUN, and D. LANDIS, "Isiscp ii modis (collection 4) igbp land cover, 2000–2001," *ORNL DAAC*, 2017.
- [70] C. Jiménez, J. Catherinot, C. Prigent, and J. Roger, "Relations between geological characteristics and satellite-derived infrared and microwave emissivities over deserts in northern africa and the arabian peninsula," *Journal of Geophysical Research: Atmospheres*, vol. 115, no. D20, 2010.
- [71] C. Prigent, J.-M. Munier, B. Thomas, and G. Ruffié, "Microwave signatures over carbonate sedimentary platforms in arid areas: Potential geological applications of passive microwave observations?" *Geophysical research letters*, vol. 32, no. 23, 2005.
- [72] R. C. Harlow and R. Essery, "Tundra snow emissivities at mhs frequencies: Memls validation using airborne microwave data measured during clpx-ii," *IEEE Transactions on Geoscience and Remote Sensing*, vol. 50, no. 11, pp. 4262–4278, 2012.
- [73] D. Wang, C. Prigent, L. Kilic, S. Fox, C. Harlow, C. Jimenez, F. Aires, C. Grassotti, and F. Karbou, "Surface emissivity at microwaves to millimeter waves over polar regions: Parameterization and evaluation with aircraft experiments," *Journal of Atmospheric and Oceanic Technology*, vol. 34, no. 5, pp. 1039–1059, 2017.

- [74] E. Cordisco, C. Prigent, and F. Aires, "Snow characterization at a global scale with passive microwave satellite observations," *Journal of Geophysical Research: Atmospheres*, vol. 111, no. D19, 2006.
- [75] M. Sturm, J. Holmgren, and G. E. Liston, "A seasonal snow cover classification system for local to global applications," *Journal of Climate*, vol. 8, no. 5, pp. 1261–1283, 1995.
- [76] S. J. Munchak, R. Meneghini, M. Grecu, and W. S. Olson, "A consistent treatment of microwave emissivity and radar backscatter for retrieval of precipitation over water surfaces," *Journal of Atmospheric and Oceanic Technology*, vol. 33, no. 2, pp. 215–229, 2016.
- [77] Y. You, C. Peters-Lidard, J. Turk, S. Ringerud, and S. Yang, "Improving overland precipitation retrieval with brightness temperature temporal variation," *Journal of Hydrometeorology*, vol. 18, no. 9, pp. 2355–2383, 2017.
- [78] J. King, C. Derksen, P. Toose, A. Langlois, C. Larsen, J. Lemmetyinen, P. Marsh, B. Montpetit, A. Roy, N. Rutter *et al.*, "The influence of snow microstructure on dual-frequency radar measurements in a tundra environment," *Remote sensing of environment*, vol. 215, pp. 242–254, 2018.
- [79] M. Stieglitz, A. Ducharne, R. Koster, and M. Suarez, "The impact of detailed snow physics on the simulation of snow cover and subsurface thermodynamics at continental scales," *Journal of Hydrometeorology*, vol. 2, no. 3, pp. 228–242, 2001.
- [80] T. Carroll, D. Cline, C. Olheiser, A. Rost, A. Nilsson, G. Fall, C. Bovitz, and L. Li, "Noaas national snow analyses," in *Proceedings of the 74th annual meeting of the western snow conference*, vol. 74, 2006, p. 13.
- [81] J. King, R. Kelly, A. Kasurak, C. Dugaay, G. Gunn, N. Rutter, T. Watts, and C. Derksen, "Spatio-temporal influence of tundra snow properties on ku-band (17.2 ghz) backscatter," *Journal of Glaciology*, vol. 61, no. 226, pp. 267–279, 2015.



S. Joseph Munchak received the B.S. and M.S. degrees in meteorology from Pennsylvania State University, University Park, PA in 2006 and the Ph.D. degree in atmospheric science from Colorado State University, Fort Collins, CO in 2010. He was a Research Associate and Assistant Research Scientist at the University of Maryland, College Park's Earth System Science Interdisciplinary Center from 2010 until 2015,

when we took his current position as a Research Meteorologist at NASA Goddard Space Flight Center. Dr. Munchak's main research interests are in the integration of passive and active microwave measurements to improve retrievals of clouds and precipitation. This work has many avenues which Dr. Munchak has engaged in current and past research investigations, including development of three-dimensional inversion methods, optimal parameterizations of rain and snow particle size distributions, development of clear-air retrievals for precipitation detection, and surface characterization for active and passive sensors.

Dr. Munchak is currently Deputy Project Scientist for Ground Validation for NASA's Global Precipitation Measurement mission and serves as an Associate Editor for *Atmospheric Measurement Techniques*. Dr. Munchak is a member of the American Meteorological Society and American Geophysical Union.



Sarah Ringerud received the B.S. degree in atmospheric and oceanic sciences and mathematics from the University of Wisconsin-Madison, in 2002, and M.S.(2006) and PhD (2015) degrees in Atmospheric Science from Colorado State University, Fort Collins. Following graduation Sarah worked as a NASA Postdoctoral Fellow at Goddard Space Flight Center in Greenbelt, Maryland, on passive microwave remote sensing of precipitation.

She is currently with the University of Maryland's Earth System Science Interdisciplinary Center, with research focusing on passive microwave precipitation retrievals over land surfaces as part of the Global Precipitation Measurement Mission Science team.



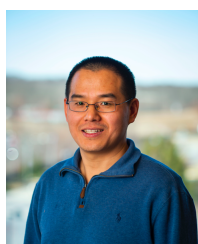
Ludovic Brucker received the M.S. degree in physics from the University of Clermont-Ferrand, France, in 2006 and the Ph.D. degree from the Laboratoire de Glaciologie et Geophysique de l'Environnement, Uni. Grenoble Alpes / Centre National de la Recherche Scientifique, Grenoble, France, in October 2009. He then joined the NASA Goddard Space Flight Center, Greenbelt, MD. His research focuses on the

investigation of climate evolution in polar regions by interpreting space-borne microwave observations of snow-covered surfaces (sea ice, ice sheet and terrestrial snowpacks). His work contributes to the comprehension of the relationships between passive microwave air- and space-borne observations and snow/ice physical properties using modeling approaches to provide climate-related variables to the community for the satellite era. To that end, he works on developing algorithms and state-of-the-art multilayer snow evolution and emission models. He has also participated in polar deployments in Antarctica, Greenland, and northern Canada.



Catherine Prigent received the Ph.D. degree in physics from Paris University in 1988. Since 1990, she has been a Researcher with the Centre National de la Recherche Scientifique, Laboratoire d'Etudes du Rayonnement et de la Matière en Astrophysique, Paris Observatory. From 1995 to 2000, she was with the NASA/Goddard Institute for Space Studies, Columbia University, New York. She is currently the Co-

Founder of Estellus, a start-up specialized in satellite Earth observations and also an Adjunct Research Scientist with the Water Center, Columbia University. She was involved in the modeling of the sea surface emissivities at microwave wavelengths and the estimation of atmospheric parameters over ocean from microwave measurements. She has authored over 120 papers in international journals, covering a large range of Earth remote sensing applications. Her current research interests include satellite microwave remote sensing of the Earth, for both surface and atmosphere characterization for global applications, the atmospheric and surface parameters over land from microwave observations using the synergy with satellite measurements at other wavelengths, key surface parameters include microwave land emissivities, all weather determination of land skin temperature, and the first estimates of the wetland extent and dynamics at global scale, and satellite remote sensing of clouds with the analysis of passive microwave and millimeter observations.



Yalei You received the B.S. and M.S. degrees in Atmospheric Science from the Yunnan University, Kunming, Yunnan, China, in 2005 and 2008, respectively, and the Ph.D. degree in Meteorology from the Florida State University, Tallahassee, FL, USA, in 2013.

He is currently an assistant research scientist at the Earth System Science Interdisciplinary Center (ESSIC), and the Cooperative Institute for Satellite

Earth System Studies (CISESS)-Maryland, University of Maryland (UMD), College Park, MD, USA. His research interest include the passive microwave precipitation algorithm development, the precipitation dataset validation, and the microwave instrument calibration. He has served as an Associate Editor for the Journal of Hydrometeorology and the Journal of Applied Meteorology and Climatology.